CHAPTER 4

Secondary Topographic Attributes

John P. Wilson and John C. Gallant

4.1 INTRODUCTION

This chapter describes four grid-based programs for calculating secondary topographic attributes: EROS, SRAD, WET, and DYNWET. These programs were originally developed by Moore (1992) and subsequently modified and added to by various contributors (Wilson and Gallant 1998). The four grid-based programs compute a series of secondary attributes that combine two or more primary attributes and can be used to characterize the spatial variability of specific hydrological, geomorphological, and ecological processes occurring in landscapes. The computed topographic attributes are based on simplified representations of the underlying physics of the processes in question but include the key factors that modulate system behavior (e.g., topography) (Moore and Hutchinson 1991). With this approach we sacrifice some physical sophistication to allow improved estimates of spatial patterns in landscapes (Moore et al. 1993d). The methods are able to handle variations in the availability of possible input data and the spatial resolution of those data. Care must be taken in developing and using these techniques because simplifying assumptions can increase rather than resolve computational complexity. This possibility looms large for systems with many variables and for models with many simplifications where several variables of the original model participate in the simplifying assumptions (Denning 1990, Moore and Hutchinson 1991, Grayson et al. 1993).

The inputs, outputs, and estimation methods employed by EROS, SRAD, WET, and DYNWET are described in the sections that follow together with an illustrative application of each program for the same Cottonwood Creek catchment introduced in Chapters 2 and 3. The programs are written in FORTRAN77 and C for Unix systems, and produce output files in the same format as TAPES-G, including metadata describing the options and parameters specified when running the programs. The file format and tools for displaying, analyzing, and converting the output files are described in Section 3.1.12.

Terrain Analysis: Principles and Applications, Edited by John P. Wilson and John C. Gallant.
ISBN 0-471-32188-5

4.2 EROS

This program calculates a pair of simple erosion indices that account for the major hydrological and topographic attributes affecting erosion (Wilson and Gallant 1996). These indices incorporate a dimensionless sediment transport capacity that is a non-linear function of specific discharge and slope (Chapter 1; Moore and Burch 1986a–c). They are derived from the transport capacity limiting sediment flux in the Hairsine–Rose (Hairsine and Rose 1991, 1992a, b), WEPP (Laflen et al. 1991a, b), and catchment evolution (Willgoose et al. 1991) erosion theories (Moore et al. 1992). Both indices can be easily extended to three-dimensional terrain, they can account for different runoff producing mechanisms and soil properties using a spatially variable weighting function, and they can be implemented within a Geographic Information System (GIS) (Moore and Wilson, 1992, 1994).

4.2.1 Estimation Methods

The first erosion index in EROS calculates the spatial distribution of soil loss potential with a simple dimensionless stream power or sediment transport capacity index, T_c, which can be written as

$$T_{cj} = \left(\frac{\sum_{i \in C_j} (\mu_i a_i)/b_j}{22.13}\right)^m \left(\frac{\sin \beta_j}{0.0896}\right)^n \tag{4.1}$$

where μ_i is a weighting coefficient ($0 \le \mu_i \le 1$) that is dependent on the runoff generation mechanism and soil properties (i.e., infiltration rates), a_i is the area of the ith cell, b_j is the width of each cell, β_j is the slope in degrees, m and n are constants (0.6 and 1.3, respectively), and C_j is the set of elements that are hydrologically connected to cell j (i.e., the catchment area of the cell, including the current cell j). When $\mu = 0$, no rainfall excess is generated on that cell; when $\mu = 1$, all of the precipitation on the cell becomes rainfall excess.

The second index represents the change in sediment transport capacity across a grid cell, ΔT_c, and provides a possible measure of the erosion or deposition potential in each cell (Moore and Burch 1986a). The change in sediment transport capacity across hydrologically connected grid cells can be written as

$$\Delta T_{cj} = \phi \left[\left(\sum_{i \in C_{j-}} \frac{\mu_i a_i}{b_{j-}} \right)^m (\sin \beta_{j-})^n - \left(\sum_{i \in C_j} \frac{\mu_i a_i}{b_j} \right)^m (\sin \beta_j)^n \right] \tag{4.2}$$

where ϕ is a constant, subscript j signifies the outlet of cell j and $j-$ signifies the inlet to cell j, and C_{j-} is the set of elements that are hydrologically connected to cell j excluding the current cell (Moore et al. 1992). Positive values of ΔT_{cj} indicate net deposition and negative values indicate net erosion.

Three options are provided in EROS for estimating the weighting coefficients in the above pair of equations. The first option assumes that rainfall excess is generated uniformly over the entire catchment (i.e., $\mu_i = \mu = 1$). The second option assumes saturation overland flow in which overland flow occurs only in zones of saturation in landscapes. The final option assumes Hortonian overland flow in which μ_i is spatially variable and a function of the infiltration characteristics of the soil (Wilson and Gallant 1996). The choice of the best option for a particular application (catchment) is difficult because the runoff production system involves the interaction of atmosphere, land geology and geomorphology, vegetation, soils, and people. The final choice of runoff method often relies on intuition and circumstantial evidence (Pilgrim and Cordery 1993).

The uniform rainfall excess method is often used because no additional knowledge of runoff behavior and infiltration rates is required. The erosion indices can be computed directly from the slope and drainage area attributes calculated in TAPES-G with simplified versions of Equations 4.1 and 4.2 in this instance:

$$T_c = \left(\frac{A_s}{22.13}\right)^m \left(\frac{\sin\beta}{0.0896}\right)^n \tag{4.3}$$

$$\Delta T_{cj} = \phi\,[A_{sj-}^m(\sin\beta_{j-})^n - A_{sj}^m(\sin\beta_j)^n] \tag{4.4}$$

where β is the slope (in degrees) and A_s is the specific catchment area or drainage area per unit width orthogonal to a flow line (m^2/m). Equation 4.3 is equivalent to the length–slope factor in the Revised Universal Soil Loss Equation (Renard et al. 1991) for planar slopes with lengths <100 m and gradients < 14°, but it is simpler to use and conceptually easier to understand (Moore and Wilson 1992, 1994). This index can also explicitly account for flow convergence and divergence, and an extension can be used to account for both detachment- and transport-limited soil loss rates (see Chapter 1 and Wilson and Lorang 1999 for additional details).

The saturation overland flow method should be selected if runoff is to be determined by surface saturation controlled by a user-specified critical wetness index. For this case, $\mu_i = 0$ when $\ln(A_s/\tan\beta) < W_c$ and $\mu_i = 1.0$ when $\ln(A_s/\tan\beta) \geq W_c$, where $\ln(A_s/\tan\beta)$ is a topographic wetness index (Chapter 1; Moore et al. 1988a) and W_c is a user-specified critical wetness index that identifies the location of zones of surface saturation in the landscape. Moore et al. (1992) used a critical wetness index of 6.0 and found that $T_c > 2.5$ showed good agreement with areas of degradation observed in a 9.6-ha catchment in Queensland, Australia during 1979–80 when vegetation was sparse. The wetness index values are calculated for each grid point and compared with the user-specified critical wetness index to determine the weights used in Equation 4.1 with this option.

The third and final (Hortonian overland flow) method incorporated in EROS should be selected if runoff is to be determined by infiltration excess. This option requires a file with two or more soil polygons and weights. The program then performs a series of point-in-polygon overlays to assign weights to individual DEM grid points. The drainage areas are recalculated using these weights, the flow directions copied from TAPES-G, and one of the D8, Rho8, or FD8/FRho8 flow-routing methods discussed in Chapter 3. The slope values copied from TAPES-G and the new drainage areas are then used to calculate T_c in Equation 4.1.

4.2.2 Inputs

EROS requires the x, y, z (elevation), slope gradient, flow direction, and drainage area attributes from TAPES-G (Chapter 3; Gallant and Wilson 1996). It looks for metadata on the input file to determine the grid cell size, missing value, and field numbers, and assumes standard TAPES-G format if there are no metadata. EROS recognizes an elevation value of 0 as a missing value, and also recognizes TAPES-G's missing value of −9999.0. It uses the same missing value in its output file. EROS assumes that the coordinates and elevation are in meters, but there is no problem using other units as long as the elevation units are the same as the units of the x and y coordinates. No additional inputs are required so long as the rainfall excess runoff method is chosen. However, the user will be asked to specify the critical topographic wetness index if the second (saturation overland flow) method is chosen, and a soil boundary file containing soil polygons and weights is required if the third (infiltration excess overland flow) option is chosen.

The critical topographic wetness index required for the second option can be estimated from the fraction of precipitation converted to runoff and a cumulative frequency plot of the steady-state topographic wetness index. The fraction of precipitation converted to runoff may be obtained from long-term rainfall–runoff records, published reports (e.g., Parrett and Hull 1985), or the U.S. Soil Conservation Service (SCS) runoff curve number method. The SCS method is sometimes used in conjunction with the WET program and is discussed in more detail in Section 4.4.2. The steady-state topographic wetness index required here can be calculated with either DYNWET or WET and plotted against catchment area (as in Figure 4.4) to identify the critical topographic wetness index for a particular catchment.

The soil boundary file required for the Hortonian overland flow option specifies (1) an integer indicating the number of soils for each model run; (2) the number of vertices, soil number, and weight for each polygon; and (3) the x, y coordinates delineating the boundary of each polygon. The second and third items are repeated for each soil polygon, and soil polygons must be labeled with integers starting from 1. The soil polygons may be able to be acquired from one of several digital geographic soil databases produced in the past few years or converted from an existing soil map to a digital file (Wilson 1999a). The weights are more difficult to acquire and will usually have to be derived by the EROS user from two additional types of information as follows.

We need to know something about the infiltration rates of soils when thoroughly wetted and the time pattern of precipitation intensity to estimate these weights. The assignment of soil series to hydrologic soil groups gives a rough guide to infiltration rates in the United States (Pilgrim and Cordery 1993, Rawls et al. 1993). More precise inputs will usually require site-specific sampling, field measurement, and interpolation. Some variant of kriging is often used with field measurements (hard data) and other (soft) data to generate soil infiltration maps for farm fields and catchments in these situations (e.g., Rogowski and Hoover 1996). Rainfall intensity information can be presented in hyetographs and it is usually assumed to be the same over all points in a catchment (Pilgrim and Cordery 1993). The time pattern of rainfall intensity can then be combined with information about the areal extent and hydrologic behavior of different soil series to estimate the proportion of runoff generated from different soil polygons and determine the final weights used with the Hortonian overland flow method in EROS.

4.2.3 Outputs

EROS produces an output file in either binary or ASCII form with metadata, as described in Section 3.1.12. Each DEM grid point with all its attributes is written to a single record as either one line in an ASCII file or one unformatted record in a binary file. The x, y, and z fields are copied from the TAPES-G input file, and the weights are determined from the soil polygons or EROS program itself. The drainage area field is similar to the drainage area calculated by TAPES-G except where it is modified by soil weights.

4.3 SRAD

This program calculates potential solar radiation as a function of latitude, slope, aspect, topographic shading, and time of year, and then modifies this estimate using information about monthly average cloudiness and sunshine hours. Temperature is extrapolated across the surface using a method based on Running et al. (1987), Hungerford et al. (1989), Running (1991), and Running and Thornton (1996) that corrects for elevation via a lapse rate, slope–aspect effects via a short-wave radiation ratio, and vegetation effects via a leaf area index. Daily outgoing long-wave irradiance is calculated from surface temperature and daily incoming long-wave irradiance is calculated from air temperature and the fraction of sky visible at each grid point. These short- and long-wave radiation fluxes are then used to estimate the surface energy budget at each grid point for a user-specified period ranging from one day to one year in length. Solar radiation is not widely measured, but the fact that the apparent solar path relative to any location and any surface can be simply and easily calculated with great accuracy suggests radiation indices can be used to compare sites (Fleming 1987). These estimates are valuable because the surface energy budget exerts a large impact on the evaporation and photosynthesis processes occurring at the land surface and is highly dependent on topography. Vegetation diversity and biomass production are related to radiation input (e.g., Austin et al. 1984, Tajchman and Lacey 1986, Moore et al. 1993e, Franklin 1995).

4.3.1 Estimation Methods

4.3.1.1 Short-Wave Radiation The general approach used by SRAD to estimate short-wave radiation at both flat and inclined sites incorporates four steps. First, the potential or extraterrestrial irradiance on a horizontal surface just outside the earth's atmosphere is calculated. Second, a series of instantaneous clear-sky, short-wave radiation fluxes is calculated for each of the DEM grid points at 12-min intervals from sunrise to sunset. Direct beam and diffuse fluxes are calculated for flat sites and direct beam, circumsolar diffuse, isotropic diffuse, and reflected fluxes are calculated for sloping sites at this stage. Third, these instantaneous values are summed to obtain daily totals and these values are adjusted to account for the effects of cloudiness. Fourth, the daily values are summed over the estimation period specified by the user and divided by the number of days to estimate average daily values in each period.

4.3.1.1.1 Extraterrestrial Radiation SRAD combines a series of fundamental angles, as defined in astronomy and related to one another by means of spherical trigonometry, with the solar constant to estimate daily amounts of direct sunlight incident on a horizontal surface just outside the earth's atmosphere. The amount of sunlight incident at a point just outside the atmosphere, R_{oh}, depends on the time of year, time of day, and latitude as follows:

$$R_{oh} = \frac{I}{r^2} \cos z \tag{4.5}$$

where I is the solar constant (see Table 4.1 for additional details), r is the ratio of the earth–sun distance to its mean, and z is the zenith angle (Gates 1980, Fleming 1987). The magnitude of r^2 varies continuously throughout the year from 1.0344 on 3 January to 0.9674 on 5 July, but never deviates more than 3.5% from 1.0 (Gates 1980). This ratio is calculated in SRAD as a function of day number.

The zenith angle is the angle between the solar beam and the normal to the surface and can be computed from the following equation:

$$\cos z = \sin \phi \sin \delta + \cos \phi \cos \delta \cos h \tag{4.6}$$

where ϕ is the latitude of the observer (degrees, negative in the southern hemisphere), δ is the declination of the sun, and h is the hour angle of the sun from solar noon (i.e., the angular distance from the meridian of the observer) (Lee 1978). The solar declination (δ) measures the seasonally varying latitude of the sun's path across the sky, north and south of the equator. It varies from −23.5° at the northern winter solstice (22 December) to +23.5° at the northern summer solstice (22 June). Declination is independent of calendar year and the latitude of the observer and is a function only of time of year (Gates 1980). The hour angle (h) measures the difference in time from solar noon expressed as 15° per hour of difference. Some authors substitute the solar elevation or altitude (a) in place of the zenith angle because this variable represents the height of the sun above the horizon for an observer at a specific location and is the complement of the zenith angle (i.e., $\sin a = \cos z$). Both the zenith angle and solar altitude are functions of latitude, time of year, and time of day (Gates 1980).

SRAD calculates instantaneous values of R_{oh} (and the other short-wave radiation fluxes described below) at time steps of 12 min organized symmetrically around noon and sums these to obtain daily totals. Fleming (1987) relied on results from

Monteith (no reference cited) and concluded that this approach yielded sufficiently accurate daily estimates for most of the types of hydrological, geomorphological, and ecological applications considered in this book. The units used for the radiation values in SRAD are chosen at run time together with the value of the solar constant from the list of options summarized in Table 4.1.

4.3.1.1.2 Direct-Beam and Diffuse Radiation at Horizontal Sites Under Clear Skies The amount of solar energy reaching the ground is reduced because the atmosphere is semitransparent to solar radiation. The molecular constituents of the atmosphere, along with water droplets, dust, and other particulate matter, scatter the direct solar beam and create a hemispherical (diffuse) source of radiant energy (Lee 1978). In addition, the direct and diffuse irradiance are both reduced as a result of direct absorption and reflection to space along the light beam's path through the atmosphere to the ground (Linacre 1992). We therefore need to know the transmission properties of the atmosphere to estimate the amount of extraterrestrial or potential direct solar radiation that traverses the earth's atmosphere and is incident at the ground (Gates 1980). Two approaches are provided in SRAD to estimate these fluxes: One uses a lumped transmittance approach and the other calculates individual transmittance components.

The lumped approach assumes that the attenuation of the direct solar beam in passing through a homogeneous, cloudless atmosphere can be described by the following formula, often named after Beer, though first formulated by Pierre Bouguer in 1760:

$$R_{\mathrm{dirh}} = R_{\mathrm{oh}}\,\tau^{m} \tag{4.7}$$

where R_{dirh} is the direct-beam, short-wave irradiance incident on flat surfaces under clear skies, τ is the transmission coefficient or fraction of radiation incident at the top of the atmosphere, which reaches the ground along the vertical (or zenith) path (i.e., the shortest path length between outer space and the ground surface), and m is the ratio of the path length in the direction of the sun at zenith angle z to the path length in the vertical direction (Gates 1980, Linacre 1992).

The local transmission coefficient for each grid cell τ is calculated in SRAD from the elevation, monthly transmission coefficient at sea level, and transmissivity lapse rate as follows:

$$\tau = \tau_{\mathrm{sl}} + t_{\mathrm{lapse}} * \mathrm{elev} \tag{4.8}$$

TABLE 4.1 SRAD Irradiance Units

Solar Constant	Corresponding Irradiance Units
1.9 cal/cm^2/min	cal/cm^2/day
119.4 langley/h	langley/day = cal/cm^2/day
4.871 MJ/m^2/h	MJ/m^2/day
1354 W/m^2	W/m^2

where τ_{sl} is the transmission coefficient at sea level, t_{lapse} is the transmissivity lapse rate, and elev is the elevation at a specific grid point. This equation mimics the common situation in which transmittance is greater at higher elevations because of the thinner layer of atmosphere that occurs above these locations (Linacre 1992). The quantity m is often called the relative air mass and is given by

$$m = \sec z = \frac{1}{\cos z} \tag{4.9}$$

where z is the zenith angle that was first used in Equation 4.5. However, this equation works only when the zenith angle is less than about 60°: When the sun is low in the sky, the curvature of the earth reduces the length of the sun's slant rays compared with the depth of the atmosphere in the zenith direction (Robinson 1966, Gates 1980). SRAD relies on the above equation when the zenith angle is less than 60° and reverts to a table obtained from List (1968, 422) that summarizes optical air masses in 1° intervals for sites at higher zenith angles. These values are then corrected to account for the reduction in atmospheric pressure encountered at higher elevations by the factor p/p_o, where p is the atmospheric pressure at the grid cell, and p_o is the standard sea level pressure of 1013.25 mbar (Gates 1980, Fleming 1987).

Equations 4.7 through 4.9 are required to estimate the attenuation of the instantaneous direct-beam, short-wave irradiance incident at the ground surface. Some of the direct-beam radiation is transformed into diffuse radiation and the relationship for instantaneous transmittance to diffuse skylight derived by Liu and Jordan (1960) is used in SRAD to estimate the instantaneous diffuse irradiance R_{difh} as follows:

$$R_{difh} = (0.271 - 0.294\,\tau^{m})R_{oh} \tag{4.10}$$

Equation 4.10 shows that the transmittance to scattered skylight decreases as the direct solar beam transmittance increases (Gates 1980). The distinction between direct-beam and diffuse short-wave irradiance is an important one and we will see shortly how it affects the amount of short-wave irradiance striking a sloping surface (Linacre 1992).

The second approach in SRAD for estimating direct-beam and diffuse short-wave irradiance on horizontal sites under clear skies treats each of the transmittance components separately. The effects of water vapor, dust, and a clear atmosphere can be estimated in SRAD as follows:

$$R_{dirh} = R_{oh}(\mathrm{AW} * \mathrm{TW} * \mathrm{TD} * \mathrm{TDC}) \tag{4.11}$$

where AW accounts for the absorption by water vapor, TW the scattering by water vapor, TD the scattering by dust, and TDC the scattering by air molecules and density fluctuations in a clear-sky atmosphere (Gates 1980). Four equations specified by Fleming (1987) and based on work by Monteith (no reference cited) and Idso (1969) were modified and are used in SRAD to estimate each of these transmittance components as follows:

$$\mathrm{AW} = 1 - 0.077 * \left[u * m\left(\frac{p}{p_o}\right)\right]^{0.3} \tag{4.12}$$

$$\mathrm{TW} = 0.975^{um(p/po)} \tag{4.13}$$

$$\mathrm{TD} = 0.95^{m(p/po)D} \tag{4.14}$$

$$\mathrm{TDC} = 0.9^{m(p/po)} + 0.026 * [m\left(\frac{p}{p_o}\right) - 1] \tag{4.15}$$

where m, p, and p_o were defined earlier, u is the water content of a vertical slice of atmosphere in centimeters, and D is an empirically derived dust factor. The original equations specified by Fleming (1987) did not correct the air masses for elevation (like we do in Equations 4.12 through 4.14) because they assumed that local dust and water vapor measurements were available. The dust factor used in Equation 4.14 is especially problematic and can be related to atmospheric turbidity such that $D = 2$ corresponds to 300 ppm dust and $D = 1$ is slightly less than 100 ppm (i.e., the standard conditions at many sites) (Fleming 1987).

The above component atmospheric transmittance model assumes that absorption takes place first followed by scattering, and that the scattering is evenly divided between forward and back scattering. The implementation of this option in SRAD tries to strike a balance between accuracy and input data requirements. As a result, several effects are ignored (i.e., absorption effects of carbon dioxide and ozone) and each of the components that is considered is treated as acting uniformly over the whole solar spectrum when we know that most of these effects are strongly wavelength dependent (Gates 1980). We have also assumed that the scattered radiation gives rise to the diffuse radiation component without further absorption so that

$$R_{\mathrm{difh}} = 0.5 * (R_{\mathrm{oh}} * AW - R_{\mathrm{dirh}}) \tag{4.16}$$

4.3.1.1.3 Circumsolar and Isotropic Diffuse Radiation Linacre (1992, 152) distinguished "skylight" diffuse radiant energy, which is isotropic (i.e., comes more or less equally from all directions in the sky), and "circumsolar" diffuse radiation, which comes from within approximately 5° of the direct solar beam. The circumsolar diffuse component moves across the sky with the sun and can be separated and added back into the direct-beam component for the calculation of the radiation incident on sloping sites (Fleming 1987). Monthly average values of the fraction of diffuse radiation that is close to the solar disk are obtained from the site-parameter file and used by SRAD to adjust the direct-beam and diffuse radiation fluxes as follows:

$$R_{\mathrm{dirh}} = R_{\mathrm{dirh}} + R_{\mathrm{difh}} * \mathrm{CIRC} \tag{4.17}$$

$$R_{\mathrm{difh}} = R_{\mathrm{difh}} - R_{\mathrm{difh}} * \mathrm{CIRC} \tag{4.18}$$

where CIRC is the fraction of diffuse radiation derived from within 5° of the direct solar beam (i.e., the circumsolar coefficient). Many other solar radiation models do not separate these components and this omission may generate errors as large as 40% when these models are used to estimate irradiance on sloping sites (Linacre 1992).

4.3.1.1.4 Direct-Beam, Diffuse, and Reflected Radiation at Sloping Sites Under Clear Skies The flux density of short-wave radiation on a sloping site differs from that on a horizontal surface primarily because the direct-beam radiation is modified. Minor differences also occur because the flux of diffuse sky radiation is affected and there is an added flux of short-wave radiation reflected from adjacent parts of the landscape (Lee 1978, Fleming 1987).

Four site attributes (slope, aspect, horizon, and skyview) are required to estimate the direct-beam and circumsolar irradiance with and without shading, the isotropic diffuse irradiance, and the reflected irradiance on sloping sites. The slope, aspect, and fraction of sky hemisphere that is visible are computed by SRAD for each grid point. The maximum slope and aspect are calculated with the same central finite difference scheme implemented in TAPES-G (see Chapter 3 for details). The one-dimensional horizon algorithm of Dozier et al. (1981) is used to estimate the fraction of the sky hemisphere, v, visible at each grid point. This algorithm constructs profiles across the DEM and determines the horizon angle, H_ϕ, for each grid point in a discrete number of directions, ϕ (usually 16). This algorithm is attractive because its computational efficiency is proportional to the number of grid points in a regular DEM. However, we modified the original algorithm to use bilinear instead of nearest-neighbor interpolation to construct the profiles because the latter method estimates erroneous horizon effects in some steeply sloping areas. The skyview fraction, v, is computed from the horizon angles, H_ϕ, by averaging the cosine of the horizon angles:

$$v = \frac{1}{n}\sum_{\phi=1}^{n} \cos H_\phi \qquad (4.19)$$

The direct beam and circumsolar diffuse radiation on sloping surfaces depend on the solar elevation and the slope's angle to the horizontal (Linacre 1992). Tilting a surface in the meridian plane north or south from the horizontal is the equivalent of going north or south in latitude by the same number of degrees (Gates 1980). In addition, the slope and aspect effects are greatest during winter in middle latitudes and they tend to become negligible toward the equator and the poles (Lee 1978).

The direct irradiance on a sloping surface without shading is calculated in SRAD using the following equations:

$$R_{dirs} = R_{dirh} \cos i \qquad (4.20)$$

$$\cos i = A + B \cos h + C \sin h \qquad (4.21)$$

$$A = \sin \delta \sin \phi \cos \beta + \sin \beta \cos \psi \cos \phi \qquad (4.22)$$

$$B = \cos \delta (\cos \phi \cos \beta - \sin \phi \cos \psi \sin \beta) \qquad (4.23)$$

$$C = \sin \beta \cos \delta \sin \psi \qquad (4.24)$$

where R_{dirh} in this instance is the direct-beam and circumsolar diffuse radiation on a horizontal surface under clear skies (i.e., as estimated with Equations 4.7 or 4.11 and 4.17), i is the angle between the beam and the normal to the slope, β is the slope angle, and ψ is the aspect (Lee 1978, Linacre 1992). Instantaneous values are calculated in 12-min time steps and these values are multiplied by 12 and summed to estimate daily direct-beam radiation on sloping surfaces without shading (R_{dirsns}). The program also checks whether the sun is obstructed at 12-min intervals and calculates the direct-beam and circumsolar diffuse radiation taking shading into account (R_{dirss}). This approach means of course that $R_{dirss} \leq R_{dirsns}$ at each sloping site.

The "isotropic" diffuse radiation on a sloping site is typically lower than that on a horizontal surface because part of the sky is obscured:

$$R_{difs} = R_{difh}\, \nu \tag{4.25}$$

where R_{difh} in this instance is the isotropic diffuse irradiance (i.e., as estimated with Equations 4.10 or 4.16 and 4.18), and ν is the sky-view factor (i.e., fraction of sky visible at a specific grid point).

The reductions in direct-beam and diffuse irradiance on sloping sites (compared to horizontal sites) may be partially offset by reflected radiation from other surfaces:

$$R_{ref} = (R_{dirh} + R_{difh})\,(1 - \nu)\,\alpha \tag{4.26}$$

where R_{dirh} is the direct-beam radiation on a horizontal surface under clear skies (i.e., as estimated with Equation 4.7 or 4.11), R_{difh} is the diffuse radiation on a horizontal surface under clear skies (i.e., as estimated with Equation 4.10 or 4.16), ν is the sky-view factor, and α is the albedo (i.e., fraction of sunlight reflected by the surface). For the sake of simplicity, this equation uses horizontal radiation values rather than attempting to sum the contributions of the spatially varying radiation within the ground-view area. The reflected radiation is calculated at 12-min intervals and summed over the day to estimate reflected radiation from foreground surfaces facing the site. An upward-facing area will see less sky and more ground (from which it receives reflected light) as it is tilted upward from the horizontal (Lee 1978). These inputs are important on many sloping sites and they can vary markedly with the type and status of the surface (Fleming 1987).

4.3.1.1.5 Effect of Overcast Skies The flux of direct and diffuse short-wave solar radiation incident at the earth's surface is highly variable and difficult to predict when the sky is partially or totally overcast (Linacre 1992). Clouds are highly variable in form, size, density, height, and duration. Very thin transparent cirrus clouds have little influence on global radiation, whereas thick, dark thunderstorm clouds may reduce radiation to ≤1% of its clear-sky value (Gates 1980). The approach used by SRAD combines daily short-wave radiation estimates for clear skies with statistical averages of observational data collected over long periods of time.

The accumulated radiation values at the end of each simulated day are combined with the sunshine fraction and cloud transmittance for the month in question to estimate daily incoming short-wave solar radiation on horizontal sites R_{th} as follows:

$$R_{th} = (R_{dirh} + R_{difh})\left[\frac{n}{N} + \left(1 - \frac{n}{N}\right)\beta\right] \tag{4.27}$$

where n/N is the sunshine fraction (i.e., the observed duration of sunshine out of the maximum possible for that place and date), and β is the cloud transmittance (i.e., the fraction of clear-sky radiation received when the sky is overcast).

For sloping sites, the cloud transmittance in SRAD is adjusted downward to account for the reduction in sky view and upward to account for the enhanced flux of downward and upward diffuse radiation caused by multiple reflection between ground and sky. Gates (1980) reports measurements by Kondratyev (1969) illustrating these effects and they are approximated in SRAD with the following equation:

$$\beta_s = \beta\nu\left(\frac{R_{tsns}}{R_{tss}}\right) \tag{4.28}$$

where R_{tsns} is the total daily clear-sky, short-wave radiation without shading and R_{tss} is the total daily clear-sky, short-wave radiation with shading on sloping sites. The daily incoming short-wave solar radiation on sloping sites, R_{ts}, is then estimated as follows:

$$R_{ts} = (R_{dirss} + R_{difs})\left[\frac{n}{N} + \left(1 - \frac{n}{N}\right)\beta_s\right] + R_{ref} \tag{4.29}$$

4.3.1.2 Temperature SRAD estimates temperatures at each grid point as a function of the mean monthly minimum and maximum air temperatures, surface temperature, minimum, maximum, and average temperature lapse rates, and elevation for a reference station (as specified in the site-parameter file). The radiation effect on temperature is introduced via the short-wave radiation ratio, S, at each grid point:

$$S = \frac{R_{ts}}{R_{th}} \tag{4.30}$$

where R_{th} and R_{ts} are the daily total or global short-wave irradiance on horizontal and sloping sites, respectively. The minimum air, maximum air, and surface temperatures, T, at each grid point are computed using

$$T = T_b - \frac{T_{lapse}(z - z_b)}{1000} + C\left(S - \frac{1}{S}\right)\left(1 - \frac{\text{LAI}}{\text{LAI}_{max}}\right) \tag{4.31}$$

where z is the elevation of the grid point, z_b is the elevation of the temperature reference station, T_b is the temperature at the reference station (monthly minimum air,

maximum air, or surface
is a constant (currently
LAI_{max} is the maximum
nal pair of equations, sin
corrections are not appli
night (Moore et al. 1993
the minimum and maxin

4.3.1.3 Long-Wave R
to predict the surface ener
earth's atmosphere and s
less than the outgoing su
wave irradiance (L_{net}) rep
The daily incoming lo
ature taking sky view int

where ε_a is the atmosphe
and cloudiness), σ is the
and ν is the sky-view fac
view factor means that th
ing sites see both the sky
the fraction of the sky th
the outgoing long-wave r
radiation from foregroun
The daily outgoing lo
perature as follows:

where ε_s is the surface em
is the surface temperature

4.3.1.4 Net Solar Rad
available at the ground su
synthesis (Dubayah 1992)
adding the incoming and

$R_{net} = (1 -$

$R_{net} = (1$

These equations follow t
energy is transferred to th

maximum air, or surface), T_{lapse} is the monthly temperature lapse rate (°C/1000 m), C is a constant (currently set to 1.0), LAI is the leaf area index at the grid cell, and LAI_{max} is the maximum leaf area index. This equation is a modification of the original pair of equations, since they were discontinuous at $S = 1$. The LAI/radiation ratio corrections are not applied to minimum temperature because these occur during the night (Moore et al. 1993e). Average air temperature is assumed to be the average of the minimum and maximum air temperatures.

4.3.1.3 Long-Wave Radiation Long-wave radiation estimates are also required to predict the surface energy budget. Long-wave radiation is emitted continuously by the earth's atmosphere and surface. The incoming atmospheric flux, L_{in}, is almost always less than the outgoing surface flux, L_{out}, and this means that the average net daily long-wave irradiance (L_{net}) represents a net loss of energy from the biosphere (Lee 1978).

The daily incoming long-wave irradiance in SRAD is computed from air temperature taking sky view into account:

$$L_{in} = \varepsilon_a \sigma T_a^4 \nu + (1 - \nu) L_{out} \tag{4.32}$$

where ε_a is the atmospheric emissivity (a function of air temperature, vapor pressure, and cloudiness), σ is the Stefan–Boltzmann constant, T_a is the mean air temperature, and ν is the sky-view factor discussed earlier (Lee 1978). The inclusion of the sky-view factor means that this equation handles both sloping and horizontal sites. Sloping sites see both the sky and adjacent terrain and the sky-view factor, ν, accounts for the fraction of the sky that is visible and the $(1 - \nu)L_{out}$ term shows how a fraction of the outgoing long-wave radiation is added to the incoming component to account for radiation from foreground obstructions.

The daily outgoing long-wave irradiance in SRAD is computed from surface temperature as follows:

$$L_{out} = \varepsilon_s \sigma T_s^4 \tag{4.33}$$

where ε_s is the surface emissivity coefficient (>0.95 for most natural surfaces) and T_s is the surface temperature (Lee 1978).

4.3.1.4 Net Solar Radiation The net solar radiation is the quantity of energy available at the ground surface to drive air and soil heating, evaporation, and photosynthesis (Dubayah 1992). The net radiation at each grid cell is estimated in SRAD by adding the incoming and outgoing fluxes for some user-specified period as follows:

$$R_{net} = (1 - \alpha) R_{th} + \varepsilon_s L_{in} - L_{out} \qquad \text{(at horizontal sites)} \tag{4.34}$$

$$R_{net} = (1 - \alpha) R_{ts} + \varepsilon_s L_{in} - L_{out} \qquad \text{(at sloping sites)} \tag{4.35}$$

These equations follow the usual approach in that R_{net} takes a positive sign when energy is transferred to the surface and a negative sign when the direction is reversed

(Lee 1978). This approach means that SRAD will generally predict $R_{net} > 0$ during the summer half-year but R_{net} can be negative in the winter months, particularly at higher latitudes and at locations facing away from the sun that receive no direct beam radiation.

4.3.2 Inputs

Two or three input files are required by SRAD to estimate the radiation fluxes and temperatures described in the previous section: (1) a square-grid DEM; (2) a site parameter file; and optionally (3) a vegetation file specifying the vegetation type present at each DEM grid point.

The DEM may consist of x, y, z triplets or just z values. The x, y, z file can have the points in any order, whereas the z file must be in row order (all columns of the first row followed by the first column of the second row, etc.) and may have the first point in the northwest or southwest corner. The z values may be either integer or floating point; if they are integer values, a scaling factor may be applied to increase the vertical resolution of the DEM. Finally, the file may be in either ASCII or binary form. The binary forms are either direct-access 2-byte integer files, unformatted integer files, or unformatted floating point files. Direct-access files contain only the data with no record delimiters. Unformatted files contain records with delimiters. ASCII files have one record per line. DEMs containing x, y, z data are expected to have one x, y, z triplet per record. Files containing only z data can have any number of z values per record as long as each row starts in a new record. Some additional processing may also be required to create a square-grid DEM prior to running SRAD (as is the case with TAPES-G) and we use ANUDEM (Hutchinson 1988, 1989b) for this purpose (see Chapters 2 and 3 for additional details). The users should also check to see that the DEM they are using fits the size limits set when SRAD is compiled. The arrays are currently set up to handle 1000 rows and 1000 columns, although the users can change these values to suit the memory space of their machine or the size of their study area (DEM). The number of rows and columns do not have to be equal.

The radiation, temperature, and surface condition parameters that must be specified in the site-parameter file vary in terms of availability and difficulty of estimation. These inputs are summarized in Table 4.2 and the discussion here emphasizes data sources and methods of estimation. McKenney et al. (1999) noted that the estimated errors associated with some of these parameters are potentially large or at worst unknown and they quantified the sensitivity of the SRAD outputs to the magnitude of the first four radiation parameters listed below. Their findings are useful because they give some idea as the relative importance of the different inputs and the level of care that is needed when estimating individual inputs.

Five sets of radiation inputs from a nearby station are required: (1) an atmospheric transmission coefficient; (2) circumsolar coefficient; (3) sunshine fraction; (4) cloud transmittance; and (5) the elevation of the reference climate station. Mean monthly or annual values can be used, although mean monthly values are preferred outside the tropics. The user must also specify whether the clear-sky atmospheric transmission coefficients at sea level for each month will be characterized by a single lumped

TABLE 4.2 Site Para

Line	Parameter
1	Latitude minin and maximu
2	Circumsolar coefficient
3	Albedo
4	Cloud transmit
5	Sunshine fracti
6	Max air tempe
7	Min air temper
8	Average surfac temperature
9	Avg air temper lapse rate
10	Min air temper lapse rate
11	Max air tempe lapse rate
12	NLAI
13	LAI
14	Max LAI
	Surface emissi
	Transmissivity rate
	Elevation of reference sta
15/16	Atmospheric transmittanc

parameter or using wa details).

The lumped transm the fraction of solar r 1992). Mountain locat Mountains, with clear Several methods have coefficients. The most clear-sky irradiance R nearby climate station

y predict $R_{net} > 0$ during
months, particularly at
it receive no direct beam

:he radiation fluxes and
e-grid DEM; (2) a site
ing the vegetation type

e x, y, z file can have the
all columns of the first
may have the first point
ther integer or floating
ed to increase the verti-
ASCII or binary form.
s, unformatted integer
contain only the data
with delimiters. ASCII
e expected to have one
any number of z values
additional processing
nning SRAD (as is the
8, 1989b) for this pur-
hould also check to see
RAD is compiled. The
ins, although the users
line or the size of their
ave to be equal.
ers that must be speci-
ifficulty of estimation.
here emphasizes data
oted that the estimated
ally large or at worst
ts to the magnitude of
re useful because they
s and the level of care

d: (1) an atmospheric
ne fraction; (4) cloud
ation. Mean monthly
preferred outside the
spheric transmission
by a single lumped

TABLE 4.2 Site Parameters Required by SRAD

Line	Parameter	Units	Description
1	Latitude minimum and maximum	Decimal degrees	North positive, south negative (the two numbers can be the same)
2	Circumsolar coefficient	None	12 monthly values (see text for details)
3	Albedo	None	Monthly values (see text for details)
4	Cloud transmittance	None	Monthly values (see text for details)
5	Sunshine fraction	None	Ratio of actual sunshine hours to theoretical maximum day length
6	Max air temperature	°C	Monthly average values
7	Min air temperature	°C	Monthly average values
8	Average surface temperature	°C	Monthly average values
9	Avg air temperature lapse rate	°C/1000 m	Monthly average values
10	Min air temperature lapse rate	°C/1000 m	Monthly average values
11	Max air temperature lapse rate	°C/1000 m	Monthly average values
12	NLAI	None	The number of leaf area index annual profiles (see text for details)
13	LAI	None	NLAI lines of monthly leaf area index for each vegetation type in sequence
14	Max LAI	None	Maximum leaf area index, typically 10
	Surface emissivity	None	Typically 0.92 to 0.99
	Transmissivity lapse rate	1/m	Typically 0.00008 (used only with lumped atmospheric transmittance model)
	Elevation of reference station	m	Required for temperature extrapolation
15/16	Atmospheric transmittance	See text	Monthly values (see text for details)

parameter or using water and dust components (see Section 4.3.1.1.2 for additional details).

The lumped transmittance coefficient is a fraction, typically 0.60–0.70, specifying the fraction of solar radiation transmitted by the atmosphere (Gates 1980, Linacre 1992). Mountain locations at high elevations, such as the Sierra Nevada and Rocky Mountains, with clear, dry skies, may have transmittances up to 0.80 (Gates 1980). Several methods have been proposed and used to estimate lumped transmittance coefficients. The most popular method incorporates three steps. First, mean monthly clear-sky irradiance R_{thcs} is estimated from total irradiance (R_{th}) measurements at a nearby climate station:

$$R_{thcs} = \frac{R_{th}}{0.35 + 0.61(n/N)} \tag{4.36}$$

where n/N is the sunshine fraction and 0.35 and 0.61 are constants that vary with latitude (Fritz and MacDonald 1949, List 1968, Fleming 1987). Second, mean monthly clear-sky irradiance is divided by extraterrestrial irradiance to estimate the fraction of extraterrestrial radiation received at this station. Third, this fraction is adjusted with a user-specified transmissivity lapse rate to obtain monthly clear-sky transmittance at sea level. We usually specify 0.00008 per meter for the transmissivity lapse rate. Other methods have used solar radiation data collected at climate stations on clear days that are pooled into monthly groups and divided by extraterrestrial irradiance (e.g., Idso 1969, McKenney et al. 1999) or empirical relationships linking atmospheric transmittance and air temperatures (e.g., Bristow and Campbell 1984).

Alternatively, the user can specify water and dust components and SRAD will calculate the transmittances using the absorption and scattering attenuation coefficients for water and dust summarized in Equations 4.11–4.15. The inputs are specified as the water content of a vertical slice of atmosphere in centimeters, typically 1.5 to 1.7, and a dust factor, where 1 represents a standard value of about 100 ppm and 2 represents a value of about 300 ppm (Fleming 1987). Idso (1969) showed there was an annual variation about the standard value of 1 for the dust component that is correlated with the cube of the monthly windspeed in Phoenix, AZ, and Fleming (1987) recommended using this correction for other semiarid environments as well. Monthly values of precipitible water and aerosol optical depth are reported for many radiation stations.

The circumsolar coefficient, CIRC (as used in Equations 4.17 and 4.18), is the fraction of diffuse radiation originating near the solar disk and is thus subject to topographic effects (slope, aspect, and shadowing). The circumsolar diffuse radiation is typically 5% of direct radiation or about 30% of the isotropic diffuse radiation when the sky is clear, yielding a typical value of 0.25 (i.e., 30/130) for the circumsolar coefficient. However, this coefficient tends to be higher in summer and lower in winter and the following equation can be used with station data to estimate mean monthly values:

$$\mathrm{CIRC} = \frac{R_{\mathrm{dirh}}}{24I} \tag{4.37}$$

where R_{dirh} is the measured mean monthly (or annual) direct irradiance in Wh/m^2, and I is the solar constant (Isard 1986, Linacre 1992).

The sunshine fraction (n/N) used in Equations 4.27 and 4.29 is the ratio of actual sunshine hours to the theoretical maximum at that latitude. These values are reported for many stations. Monthly sunshine hour totals are recorded and can be divided by the maximum number of sunshine hours computed from duration of daylight tables to obtain this fraction in other instances (List 1968, Lee 1978).

The cloud transmittance, β, that appears in the same equations records the ratio of actual radiation to clear-sky radiation during cloudy periods on an average monthly basis. This fraction is seldom reported but can be estimated from total solar irradiance, clear-sky irradiance, and the sunshine fraction as follows:

$$R_{\text{th}} = R_{\text{thcs}}\left[\frac{n}{N} + \beta\left(1 - \frac{n}{N}\right)\right] \tag{4.38}$$

This approach sets the actual radiation equal to the sum of clear-sky radiation during bright, cloud-free periods (given by n/N) plus some fraction (β) of the clear-sky radiation during cloudy periods ($1 - n/N$). Setting $\beta = 1$ implies that cloudiness does not diminish actual radiation, whereas setting $\beta = 0$ implies that there is no radiation at all during cloudy periods. The actual value lies somewhere between these extremes and is related to the diurnal pattern of cloudiness and average density of cloudiness. Many sites exhibit large monthly variations in terms of cloudiness and the use of site-specific monthly values in place of annual averages will usually produce superior results.

Four sets of temperature inputs from a nearby station are also required for this site-parameter file: (1) minimum and maximum air temperatures; (2) surface temperature; (3) minimum, average, and maximum temperature lapse rates; and (4) the elevation of the reference climate station (Table 4.2). The larger number of climate stations recording temperature information will usually mean that this reference station is different from that used for the radiation inputs. Mean monthly or annual values can be used, although mean monthly values are once again preferred outside the tropics. These inputs are required to predict the spatial variations in both of the longwave radiation components and net solar radiation.

The mean monthly minimum and maximum air temperatures can be obtained from climate station records. Mean monthly surface temperature is measured at a small number of these stations (Paetzold 1988) and these values will often have to be inferred from either air temperatures and other climatic variables (e.g., Toy et al. 1978) or satellite data (e.g., Brakke and Kanemasu 1981). The mean monthly average daylight, minimum, and maximum temperature lapse rates will have to be estimated from station data as well. These lapse rates vary with season and between different regions (Baker 1944, Glassy and Running 1994). Baker (1944), for example, reported maximum, average, and minimum temperature lapse rates of 6.8, 5.9, and 2.9°C per 1000 m for July, and a single value (2.9°C per 1000 m) for all three lapse rates in January in the mountains of the western United States.

We often use a modified version of a spatial filtering-kernel convolution method (Running and Thornton 1996) with local station data to estimate site-specific mean monthly average daylight, minimum, and maximum temperature lapse rates. This method incorporates a spatial filtering kernel of circular extent and fixed diameter to select a list of qualifying stations and assign weights to each station. There is one point in these regressions for each pair of stations and the weight associated with each regression point is defined as the product of the two individual station weights. The individual station weights, V_{ij}, are defined by

$$V_{ij} = e^{\left(\frac{-D_{ij}^2\alpha}{R_k^2}\right)} - e^{-\alpha} \tag{4.39}$$

where R_k is the radius of the circular kernal, D_{ij} is the distance from a qualifying climate station to the center of the kernal grid (i.e., the climate station used for the other temperature inputs), and α is a shape parameter. Running and Thornton (1996) computed the average station density (one station per 1500 km^2) and set $R_k = 201$ km and $\alpha = 4.0$ in Montana. Equation 4.39 defines a Gaussian weighting function within the circular kernel with the greatest weight located at the center of the kernel (0.982) and the weight decreasing radially outward until, at a distance, R_k, from the center of the kernel grid, the weight is zero. The independent variable in the regression is the difference in elevation between the stations in a pair, and the dependent variable is the difference in either mean monthly daylight average, minimum, or maximum temperatures between a pair of stations. Mean monthly maximum and minimum temperatures can be obtained from station records and mean monthly average daylight temperatures can be estimated from these values by assuming that the diurnal daylight trace has a sine form similar to Running et al. (1987). The weights assigned to station pairs must be summed and normalized to that sum prior to building the regression models (Running and Thornton 1996).

Four sets of parameters describing surface conditions must also be specified in the site-parameter input file: (1) the number of leaf area index profiles (NLAI), (2) one or more leaf area index profiles, (3) surface emissivity, and (4) albedo (Table 4.2). The NLAI parameter indicates the number of vegetation types in the optional vegetation type file. This vegetation file (if used) is a grid matching the dimensions of the DEM and should contain, for each grid cell, a type number between 1 and NLAI. This number selects the LAI profile that is to be used by SRAD at each grid cell. The site-parameter file must therefore contain NLAI lines of monthly LAI values. Only one LAI profile is required and used for the whole DEM if no vegetation file is specified (i.e., as in Table 4.7). LAI records the ratio of leaf area to ground cover and is usually estimated from remotely sensed multispectral reflectance data. These values and the maximum leaf area index (we usually specify $LAI_{max} = 10.0$) are used to extrapolate temperature across the DEM because the magnitude of the temperature differences will be modified by the characteristics of the energy exchange surfaces on slopes (McNaughton and Jarvis 1983). Air temperature may be increased by 2°C when a sunward-facing slope of LAI = 1.0 receives twice as much radiation as a flat surface, but the same site may experience no increase when it is assigned a LAI = 5.0 (Running et al. 1987).

The SRAD user must also specify a single surface emissivitity (ε_s) value. Many authors have calculated the mean annual emissivities for common surface types and a single value is used in SRAD because most vegetated surfaces have emissivitities that exceed 0.95 (Lee 1978, Henderson-Sellers and Robinson 1986, Oke 1987). The albedo is the fraction of sunlight reflected from the surface. Lee (1978), List (1968), Iqbal (1983), Henderson-Sellers and Robinson (1986), and Oke (1987) list typical albedo estimates for common surface types. These values range from 0.05 for moist, dark, ploughed earth to 0.90 for fresh, dry snow. Typical values include 0.18–0.25 for most agricultural crops and natural vegetation less than 1 m in height, 0.05–0.15 for coniferous forest, and 0.15–0.20 for deciduous forest (Oke 1987). Houghton (1954) calculated a planetary albedo of 0.34 with a minimum of 0.28 in the subtropics and a maximum of 0.67 at the poles. Mean monthly values should be used in SRAD for midlatitude and high-elevation sites that are covered by snow for part of the year because typical albedo values for snow-covered vegetation may be two to four times higher than summer values (Iqbal 1983). Annual averages (i.e., the same value for each month) may be used in snow-free sites dominated by evergreen vegetation.

When used over large areas, both the estimation of temperature by a lapse rate and the use of uniform cloud conditions are likely to cause substantial errors. To overcome this, the sunshine fraction and temperature parameters can be specified by raster files rather than as single values. The line in the parameter file that would otherwise specify the parameter values is replaced with a line specifying the file name, number of rows, number of columns, cell size, and the x and y coordinates of the center of the lower left (southwestern) cell. The parameter grids may be at different resolutions than the DEM, in which case the value for each DEM grid point is calculated from the parameter grid by bilinear interpolation. Each parameter file must contain one complete grid representing the parameter surface for each calendar month. When a temperature parameter is specified using a grid file, SRAD assumes that the elevation effects are accounted for in that file so the corresponding lapse rate is not required and should be omitted from the parameter file. Temperature corrections due to short-wave radiation ratio are still applied. The sunshine hours parameter surface can be derived from surfaces of monthly average radiation on a horizontal surface: Hutchinson et al. (1984) describes the generation of a radiation surface by interpolation of measured stations, with a transformed rainfall surface providing an index of cloudiness. Gallant (1997) describes an application of SRAD using grids for sunshine hours and temperatures.

McKenney et al. (1999) identified the radiation parameters that had the greatest influence on model output in the Rinker Lake region of Ontario, Canada. They calculated the annual average sunshine fraction from measured sunshine totals, the cloud transmittance from measured radiation data, and the lumped atmospheric transmittance and circumsolar coefficient (using similar methods to those reported here) and used SRAD to predict the global short-wave irradiance. Low and high values were then chosen for each input parameter (one at a time) and eight model runs were performed to quantify the sensitivity of the model output to individual input parameters.

The results were presented as a series of bar graphs that showed overall performance but not grid point by grid point variability (McKenney et al. 1999). Increasing the sunshine fraction and the cloud transmittance from 0.10 to 0.80 (their best site-specific estimates for these two parameters were 0.46 and 0.36, respectively) increased the mean average daily irradiance approximately 250 and 150%, respectively. Increasing the atmospheric transmittance from 0.50 to 0.80 (their best estimate was 0.71) increased the mean average daily irradiance approximately 150%. Increasing the circumsolar coefficient from 0.01 to 0.50 (their best estimate was 0.18) decreased the mean average daily irradiance very slightly. These results seem intuitively correct and match our expectations. Hence, large sunshine fractions imply high frequencies of clear skies, high cloud transmittances imply less dense cloud cover (i.e., less attenuation of direct beam radiation), and the higher atmospheric transmittance indicates less attenuation of direct beam radiation as well. Similarly, the lack of variation in mean average daily irradiance when the circumsolar coefficient was varied is not surprising. This result may be a function of the method of presentation, since this variable would be expected to have markedly different impacts at different sites (depending on slope, aspect, and topographic shading), and its effects may be partially offset by increases in reflected radiation.

Overall, these results indicate that SRAD users should try their best to find or estimate site-specific monthly values for the first three radiation inputs. McKenney et al. (1999) also examined the effect of varying the resolution of the DEM on model output. They used 20- and 100-m DEMs and compared mean daily short-wave irradiance estimates at common x, y grid points. The outputs displayed similar means but the range of estimates was much greater for the 20-m DEM, and in that sense they matched the results obtained in other studies comparing geographic data sets incorporating varying levels of generalization (e.g., Wilson et al. 1996). McKenney et al. (1999) also noted that the computing requirements for the higher resolution DEM and a study area the size of Rinker Lake (900 km^2) were substantial and they concluded that a 100-m DEM would probably be sufficient for many large-area ecological applications.

4.3.3 Outputs

SRAD writes the 14 attributes listed in Table 4.3 to the output file in either ASCII or binary form with metadata as described in Section 3.1.12. Each DEM grid point with all its radiation attributes is written as a single record as either one line in an ASCII file or one unformatted record in a binary file.

4.4 WET

This program predicts soil-water content taking four components of the water balance at the surface into account: precipitation, evaporation, deep drainage, and runoff. Evaporation and deep drainage are both treated as losses, and deep drainage does not contribute to base flow. Runoff comprises both surface and subsurface runoff. The long-term average water balance is estimated using an equilibrium approach and spatially uniform mean precipitation rate. These estimates are important because the soil-water content is one of the limiting factors for plant growth and is also a factor in soil formation and other geomorphological processes (I. D. Moore et al. 1991, 1993b, c). Estimating soil-water content at fine resolution across a large area is a difficult task because of the complex interactions between topography, precipitation, radiation, evaporation, and the movement of water through the soil. In addition, soil-water content and related soil properties may exhibit substantial variability over distances of 1–100 m (e.g., Brutsaert 1986, Sharma et al. 1987). The approach taken in WET is to use simple but physically realistic relationships to capture the dominant topographic influences on long-term average relative soil-water content.

Given this approach, WET can operate at three levels of complexity. At the simplest level (which we shall call level 1), radiation effects are not accounted for and the fraction of precipitation lost through evaporation and deep drainage is assumed to be spatially invariant and is specified by the user. The most complex analysis (level 3)

unction of the method of
have markedly different
opographic shading), and
adiation.
/ their best to find or esti-
ı inputs. McKenney et al.
ıe DEM on model output.
hort-wave irradiance esti-
ar means but the range of
sense they matched the
ets incorporating varying
' et al. (1999) also noted
EM and a study area the
uded that a 100-m DEM
pplications.

t file in either ASCII or
h DEM grid point with
r one line in an ASCII

ts of the water balance
drainage, and runoff.
eep drainage does not
ubsurface runoff. The
um approach and spa-
rtant because the soil-
is also a factor in soil
t al. 1991, 1993b, c).
ırea is a difficult task
cipitation, radiation,
ition, soil-water con-
ity over distances of
h taken in WET is to
ominant topographic

ıplexity. At the sim-
ccounted for and the
ıge is assumed to be
x analysis (level 3)

TABLE 4.3 SRAD Output File Fields

Field	Field Name	Units	Description
1	X	m	x coordinate
2	Y	m	y coordinate
3	Elevation	m	From DEM
4	Short-wave irradiance ratio	None	The ratio of total short-wave irradiance on the sloping surface (R_{tss}) to total short-wave irradiance on a horizontal surface (R_{th})
5	Short-wave irradiance on sloping surface	See Table 4.1	The total short-wave irradiance on the sloping surface corrected for cloud effects and topographic shading (R_{tss})
6	Short-wave irradiance on horizontal surface	See Table 4.1	The total short-wave irradiance on a horizontal surface corrected for cloud effects but not including topographic shading (R_{tsns})
7	Incoming atmospheric long-wave irradiance	See Table 4.1	L_{in}
8	Outgoing surface long-wave irradiance	See Table 4.1	L_{out}
9	Net long-wave irradiance	See Table 4.1	Absorbed incoming long-wave less outgoing long-wave irradiance ($L_{net} = \varepsilon_s L_{in} - L_{out}$)
10	Net irradiance	See Table 4.1	Sum of absorbed short-wave irradiance on sloping surface and net long-wave irradiance (R_{net})
11	Max air temperature	°C	Average maximum air temperature over the analysis period
12	Min air temperature	°C	Average minimum air temperature
13	Avg air temperature	°C	The average of the minimum and maximum air temperatures
14	Surface temperature	°C	Average surface temperature

uses spatially varying net radiation to compute potential evaporation at each grid cell and then determines soil-water content using a set of functional relationships between soil-water content, evapotranspiration, and deep drainage. Both evaporation and deep drainage are dependent on soil-water content using this level 3 analysis. At the intermediate level 2, net radiation is still used to compute potential evaporation but soil-water content is not used to modify the loss rates. Both evaporation and deep drainage proceed at their maximum rate in all grid cells regardless of water content, essentially simulating conditions of maximum soil-water content. The estimation methods, inputs, and outputs at each of these levels are described in more detail below.

4.4.1 Estimation Methods

WET is based on the assumption that the spatial distribution of soil-water content is controlled by the topographic wetness index:

$$\omega = \ln\left(\frac{A_s}{\tan\beta}\right) \tag{4.40}$$

where A_s is the specific catchment area (catchment area draining across a unit width of contour; m^2/m) and b is the slope angle (in degrees). ω is also called the wetness index, topographic index, compound topographic index, and probably other names: We prefer topographic wetness index because the index is intended to represent the topographic control on soil wetness. However, this equation incorporates at least seven key assumptions and limitations (Beven and Kirkby 1979, Moore and Hutchinson 1991, Barling et al. 1994) as follows.

First, this approach assumes that the steady-state downslope subsurface discharge is the product of average recharge and specific catchment area. Second, it assumes that the local hydraulic gradient can be approximated by local slope. Third, it assumes that the saturated hydraulic conductivity of the soil is an exponential function of depth. Fourth, it assumes steady-state conditions. However, the velocity of subsurface flow is sufficiently small that most points in a catchment receive contributions from only a small proportion of their total upslope contributing area, and the subsurface flow regime is in a state of dynamic nonequilibrium (Barling 1992). Barling et al. (1994) proposed a dynamic wetness index, which replaces A_s in Equation 4.40 with an effective specific catchment area based on both topography and drainage time as discussed in Section 4.5 (this variant has not yet been incorporated in the WET program). Fifth, this particular form of the topographic wetness index also assumes spatially uniform soil properties (in particular transmissivity), but this assumption has been justified by Wood et al. (1990), who concluded that the topographic component of the index dominates over the soil transmissivity at the subcatchment scale. Another form of the topographic wetness index that includes transmissivity variations is discussed in Chapter 1. Furthermore, the spatial distribution of topographic attributes may capture the spatial variability of soil properties at the mesoscale because pedogenesis of the soil catena often occurs in response to the way water moves through the landscape in areas with uniform parent material (Moore and Hutchinson 1991). Sixth, this approach implies that the locations in a catchment with the same value of the topographic wetness index will also have the same relationship between the local depth to the water table and the mean depth. Finally, this approach also implies that those points with the same value of the topographic wetness index will respond in a similar way to the same inputs.

The specific catchment area, A_s in Equation 4.40, is calculated using either the D8 or Rho8 algorithm as used by TAPES-G (Chapter 3; Gallant and Wilson 1996). This algorithm can be expressed as

$$A_s = \frac{\sum_{j \in C_j} a_i}{b_j} \tag{4.41}$$

where a_i is the area of the ith grid cell, b_j is the width of the jth cell, and C_j represents all of the cells upslope of cell j that are hydraulically connected to cell j (the cell's catchment area). The hydraulic connectivity is based on the flow directions determined by either the D8 or Rho8 algorithm in TAPES-G.

(4.40)

draining across a unit width
ω is also called the wetness
, and probably other names:
: is intended to represent the
juation incorporates at least
y 1979, Moore and Hutchin-

slope subsurface discharge is
a. Second, it assumes that the
pe. Third, it assumes that the
ial function of depth. Fourth,
of subsurface flow is suffi-
tributions from only a small
subsurface flow regime is in
ing et al. (1994) proposed a
.40 with an effective specific
e as discussed in Section 4.5
ogram). Fifth, this particular
ially uniform soil properties
een justified by Wood et al.
the index dominates over the
n of the topographic wetness
Chapter 1. Furthermore, the
the spatial variability of soil
soil catena often occurs in
n areas with uniform parent
ch implies that the locations
ness index will also have the
table and the mean depth.
the same value of the topo-
same inputs.
lculated using either the D8
lant and Wilson 1996). This

(4.41)

e jth cell, and C_j represents
nnected to cell j (the cell's
the flow directions deter-

Equations 4.40 and 4.41 can be generalized to account for the effects of water loss by modifying the area of each cell by a weighting factor, μ_i, dependent on the water balance at each cell:

$$A_s = \frac{\sum_{i \in c_j} \mu_i a_i}{b_j} \tag{4.42}$$

WET uses a weighting coefficient based on precipitation (P), evapotranspiration (E), and deep drainage (D):

$$\mu = 1 - \frac{E + D}{P} \tag{4.43}$$

in which E, D, and P all have units of millimeters/day. The term $(E + D)/P$ is the fraction of precipitation not converted to runoff.

The different levels of analysis in WET correspond to different methods of computing the E and D terms in Equation 4.43. The level 1 analysis allows the user to specify an $(E + D)/P$ ratio that is applied to the whole area being analyzed. This approach assumes that evapotranspiration and deep drainage do not vary across the landscape and that the only topographic control on soil water is approximated by the wetness index (i.e., Equation 4.40). The $(E + D)/P$ ratio for a catchment can be estimated directly from long-term catchment precipitation and runoff records (as described in Section 4.4.2).

The level 2 analysis incorporates spatially varying net radiation as computed by SRAD to determine the potential evapotranspiration, E_p, at each grid cell. This is used for E and the maximum deep drainage rate specified in the site parameter file is used for D. This pair of assumptions correspond to a permanently saturated surface. Potential evapotranspiration is computed using the function proposed by Priestley and Taylor (1972) for evaporative demand from well-watered vegetation under conditions of minimal advection:

$$E_p = \frac{\alpha_e (R_n - G)}{\lambda(1 + \gamma/\Delta)} \tag{4.44}$$

where R_n is the net radiation, G is the soil heat flux (which can be ignored for periods longer than one day), α_e is an empirical constant (=1.26), λ is the latent heat of vaporization of water, Δ is the slope of the saturated vapor pressure curve, and γ is the psychrometric constant (Δ and γ are functions of air temperature and pressure; see Shuttleworth (1993) or another similar work for details). The assumptions used to develop this equation are equivalent to the assumptions used in the Bowen ratio method of measuring evaporation (Shuttleworth 1993), and the corresponding Bowen ratio (the ratio of sensible to latent heat fluxes), $[(R_n - G - \lambda E_p) / \lambda E_p]$ is

$$B_0 = \frac{1 + \gamma/\Delta}{\alpha_e} - 1 \tag{4.45}$$

WET calculates and reports this Bowen ratio and allows the user to alter it if reliable information on the Bowen ratio for saturated surfaces in the study area is available. Note that the Bowen ratio is for saturated surfaces and the evaporation computed from it will be reduced for unsaturated soils when using level 3 analysis. If using level 2 analysis where no soil-water corrections are made to evaporation, a higher Bowen ratio could be supplied if sufficient data are available to determine an average Bowen ratio for the study area.

The level 3 analysis uses the same function to compute potential evapotranspiration but computes actual evapotranspiration, E, as a function of relative soil-water content and potential evapotranspiration. Various functional forms have been proposed to describe this relationship. We use the following parametrically efficient relationship proposed by Kristensen and Jensen (1975), which produces a range of responses under different evaporative demands:

$$E = E_p\,[1 - (1 - \theta)^{C/E_p}] \qquad \text{for } 0 \le \theta \le 1 \tag{4.46}$$

where θ is the relative available soil-water content (ranging from 0.0 to 1.0), E_p is the evaporative demand (mm/day), and C is a constant (about 12 mm/day). θ is determined from the topographic wetness index using one of the following relationships:

$$\theta = \frac{\omega}{\omega_{cr}} \qquad \text{for } \omega < \omega_{cr} \tag{4.47}$$

$$\theta = 1 \qquad \text{for } \omega \ge \omega_{cr} \tag{4.48}$$

The ω_{cr} term used in this last pair of equations is a user-specified critical wetness index corresponding to $\theta = 1.0$ (field capacity). Deep drainage is also made dependent on θ using a standard power-law relationship for hydraulic conductivity (Rawls et al. 1993) with the maximum deep drainage value taking on the role of saturated hydraulic conductivity:

$$D = D_{max}\theta^{\beta} \tag{4.49}$$

where β is typically between 10 and 15 (Table 4.4).

Because of the implicit relationship $\omega \rightarrow \theta \rightarrow E, D \rightarrow \mu \rightarrow \omega$, an iterative scheme is required to determine ω. WET uses a Newton–Raphson procedure for each cell, starting with cells to which there are no upslope connections (i.e., the tops of hills and ridge lines) and proceeding downslope until all cells are resolved.

4.4.2 Inputs

WET requires output files from two other programs: TAPES-G and SRAD (except for the simplest level 1 analysis where SRAD output is not required). TAPES-G provides slope and flow directions and SRAD provides net radiation estimates for each grid point. WET also requires a small number of site parameters for the study region (Table 4.4). These requirements vary with the level of analysis (1, 2, or 3) that is chosen.

One site parameter, the critical wetness index, is required for all model runs (irrespective of the level of analysis that is chosen). The choice of critical wetness index will affect the magnitude of the relative soil-water content and number of cells that

level 3 analysis. If using
to evaporation, a higher
e to determine an average

potential evapotranspira-
ion of relative soil-water
ial forms have been pro-
; parametrically efficient
hich produces a range of

≤ 1 (4.46)

from 0.0 to 1.0), E_p is the
12 mm/day). θ is deter-
following relationships:

(4.47)

(4.48)

pecified critical wetness
ge is also made depend-
ulic conductivity (Rawls
on the role of saturated

(4.49)

$\rightarrow \omega$, an iterative scheme
procedure for each cell,
ns (i.e., the tops of hills
resolved.

G and SRAD (except for
ed). TAPES-G provides
estimates for each grid
r the study region (Table
or 3) that is chosen.
for all model runs (irre-
f critical wetness index
nd number of cells that

TABLE 4.4 Site Parameters Required by WET

Parameter	Units	Levels	Description
Critical wetness index, ω_{cr}	None	All	The wetness index corresponding to maximum soil-water content (field capacity), typically 8 to 10
Mean air temperature	°C	2 and 3	Mean air temperature for the period of the analysis, recorded at a location within or near the study area
Mean elevation	m	2 and 3	The elevation of the site from which the mean temperature was recorded
Precipitation	mm/day	2 and 3	Mean precipitation over the study area for the period of analysis
Interception losses	mm/day	2 and 3	Amount of precipitation that does not reach the ground because of interception by vegetation; can be set to zero if not known
Maximum drainage rate, D_{max}	mm/day	2 and 3	The rate at which water is lost by deep drainage when the soil is fully wet (at field capacity)
β	None	2 and 3	The exponent used to relate the soil-water content to drainage rate (Equation 4.49), typically 7 (sandy soils) to 15 (clay soils)
C	mm/day	3	The exponent used to relate the soil-water content to actual evaporation rate (Equation 4.46), typically 10 to 12 mm/day
$(E+D)/P$ ratio	None	1	The fraction of precipitation lost from the soil and not converted to runoff

are saturated. The higher the critical wetness index, the lower the relative soil-water content and the fewer the number of cells classified as saturated.

The only other parameter required for the level 1 analysis is the fraction of precipitation in a catchment that is converted to runoff. This number can be determined from long-term rainfall–runoff records, or the United States Soil Conservation Service (SCS) runoff curve number model (Rawls et al. 1993). When rainfall and runoff records are available, the water balance equation

$$P = R + E + D \tag{4.50}$$

can be used directly, with P being the average annual precipitation and R the average annual runoff. Rearranging Equation 4.50 gives $E + D = P - R$, so

$$\frac{E+D}{P} = \frac{P-R}{P} \tag{4.51}$$

The SCS runoff curve number model can be used to estimate runoff from precipitation and estimates of surface condition. The model estimates runoff as

$$Q = \frac{(P - I_a)^2}{(P - I_a) + S} \tag{4.52}$$

where Q is the runoff (cm), P is the rainfall (cm), S is the potential maximum retention after runoff begins (cm), and I_a is the initial abstraction (cm) for the period (month, season, year, etc.) in question (Rawls et al. 1993).

The retention term in Equation 4.52 is highly variable from one catchment (storm) to the next and accounts for the water retained in surface depressions, water intercepted by vegetation, evaporation, and infiltration. It is often estimated with an empirical equation that was derived from data for many small agricultural catchments (Rawls et al. 1993):

$$I_a = 0.2S \tag{4.53}$$

Substituting this equation in Equation 4.52 gives

$$Q = \frac{(P - 0.2S)^2}{P + 0.8S} \tag{4.54}$$

where the parameter S is related to the soil and cover conditions of the catchment through the curve number CN:

$$S = \frac{1000}{\mathrm{CN}} - 10 \tag{4.55}$$

The major factors that determine CN are the hydrologic soil group, cover type, hydrologic condition, treatment, and antecedent runoff condition. In general, the fraction of precipitation converted to runoff will increase as infiltration rate and vegetation cover decrease. Four hydrologic soil groups (labeled A [high-infiltration soils] through D [low-infiltration soils]) and three hydrologic conditions (labeled Poor, Fair, or Good) are usually assigned. These attributes have been determined for most of the soils in the United States and can be obtained from county soil reports for most areas. For other locations, interested readers should consult Rawls et al. (1993) and the U.S. Soil Conservation Service (1985, 1986) for more detailed directions on how to determine the factors affecting CN since these decisions can have a large impact on the final runoff estimates. Composite CN estimates are sometimes computed for catchments containing distinctive soil and land cover map units.

Rawls et al. (1993) have also warned that good judgment and experience based on stream gauge records is often needed to adjust CNs as match local conditions. Pilgrim and Cordery (1993, 9.25–9.26) repeated this advice after summarizing the results of several studies that cast doubt on the accuracy and validity of the SCS method. Mancini and Rosso (1989) showed how the size and spatial arrangement of map units can affect the overall value of CN and the resulting calculated runoff when composite values of CN are estimated because of the nonlinearity of Equations 4.52 and 4.54. The SCS method should be used only when direct runoff dominates the hydrologic response of a catchment because the rainfall–runoff relationship is sensitive to surface soil-water content and the dominant runoff processes operating in the catchment. These relationships can cause problems because of the complex nature of the runoff production system (see Section 4.2.1 for additional details).

For level 2 analysis, six parameters are required in place of the $(E + D)/P$ fraction: mean air temperature from a nearby climate station, elevation of the climate station, mean precipitation, storage deficit, maximum drainage rate, D_{max}, and the exponent β in Equation 4.49 (Table 4.4). The mean air temperature and mean precipitation for the period of interest can be estimated from long-term records for a nearby station. The temperature and reference elevation values are used in the calculation of the Bowen ratio (i.e., Equation 4.45). The storage deficit, maximum drainage rate, and exponent β can be estimated from local knowledge and/or published reports (see Moore et al. (1993e) and Section 4.5 for examples). Selecting larger values for the storage deficit and maximum drainage rate will reduce the relative soil-water content (varying one input at a time). Choosing larger values of β will reduce the deep drainage losses and thereby increase the relative soil-water content.

The level 3 analysis requires one additional exponent (C) that relates the soil-water content to the actual evapotranspiration rate in addition to the one input parameter required at all three levels and the six input parameters required for the level 2 analysis (Table 4.4). We typically set C = 12 mm/day. Larger values of C will increase the actual evapotranspiration estimated with Equation 4.46 and thereby reduce the magnitude of the relative soil-water content (assuming everything else is held constant).

4.4.3 Outputs

WET produces an output file in either ASCII or binary form with metadata as described in Section 3.1.12. The computed topographic attributes for each DEM grid point are written as one line in an ASCII file or one unformatted record in a binary file. The attributes written to this file are summarized in Table 4.5. Note that there are six fields in the output file from a level 1 analysis, eight from level 2, and 10 from level 3.

4.5 DYNWET-G

This program calculates a spatially distributed topographic wetness index based on either a steady-state or quasi-dynamic subsurface flow assumption using terrain attributes computed by TAPES-G (Moore 1992). A contour-based version of the program, DYNWET-C, uses the outputs of TAPES-C and is based on the same princi-

TABLE 4.5 WET Output File Fields

Field	Field Name	Units	Levels	Description
1, 2	X, Y	m	All	x and y coordinates as specified in TAPES-G file
3	Elevation	m	All	Elevation from TAPES-G file
4	Topographic wetness index	None	All	The topographic index used to determine soil-water content, modified by losses through evapotranspiration and deep drainage
5	Relative soil-water content	None	All	Soil-water content as a fraction of field capacity; the minimum value of 0 indicates very dry soil and the maximum value of 1 indicates wet soil
6	Effective drainage area	m^2	All	The area upslope of the grid cell, reduced to account for water loss by evapotranspiration and deep drainage
7	Potential evapotranspiration	mm/day	2 and 3	The evapotranspiration under non-limiting soil-water conditions (maximum soil wetness)
8	Runoff	None	2 and 3	The water running off the grid cell to the downslope grid cell, equal to the precipitation rate multiplied by the effective drainage area, less actual evapotranspiration and deep drainage
9	Actual evapotranspiration	mm/day	3	The water lost from the grid cell by evapotranspiration, computed from potential evapotranspiration and the relative soil-water content
10	Deep drainage	mm/day	3	The water lost from the grid cell by deep drainage, computed from the maximum deep drainage rate and the relative soil-water content

ples as DYNWET-G, but will not be described in detail. The role of the wetness index in characterizing the spatial distribution of soil-water content and the location of zones of surface saturation (i.e., zones of partial area runoff) was noted earlier (see Chapter 1 and Section 4.4 of this chapter for additional details). The steady-state assumption incorporated in WET implies that the specific catchment area is an appropriate surrogate for the subsurface flow rate. This will be true only if the recharge to the surface horizons occurs at a constant rate for the length of time

required for every po
(Moore 1992, Moore
that we are most like
approach and soil-wa
rainfalls keep the soil
that the lowest points
sistently decreases as
these types of enviror
In drier environme
will receive contributi
area and the subsurfa
librium (Barling et al
days of continuous re
based on soil saturate
1967). Over shorter t
downslope in very na
play an important rol
mation of zones of so
hillslope near Wagga
flow was affected by
during storm events a
with the largest ln(A_s/
The quasi-dynami
alternative index that
rarely, if ever, reache
from its entire upslop
ment area A_e that is li
wetting events. Barli
dynamic topographic
results with the obs
sources areas. The res
wetness indices (R^2 =
days) and that the me
tribution of the quasi-
tion of spatially an
topographic wetness
scapes, although mor
types of landscapes.

4.5.1 Estimation

DYNWET calculates
4.40) based on A_s and
catchment area, A_e. T
subsurface flow:

required for every point in the catchment to reach subsurface drainage equilibrium (Moore 1992, Moore et al. 1993f, Barling et al. 1994). This state of affairs suggests that we are most likely to find a good relationship between the WET equilibrium approach and soil-water content in humid regions where frequent and substantial rainfalls keep the soil in a wet condition (e.g., Troch et al. 1993). We are likely to find that the lowest points in the catchment are the wettest and that soil-water content consistently decreases as flow lines are retraced upslope toward the catchment divide in these types of environments.

In drier environments, the velocity of subsurface flow is so small that most points will receive contributions from only a small proportion of their upslope contributing area and the subsurface flow regime is characterized by a state of dynamic nonequilibrium (Barling et al. 1994). For example, a 300-m-long slope would need 60–120 days of continuous recharge for every point to reach subsurface drainage equilibrium based on soil saturated hydraulic conductivities of 0.1–0.2 m/h (Kirkby and Chorley 1967). Over shorter time periods, the subsurface flows will only increase linearly downslope in very narrow zones close to the drainage divide and local features will play an important role in determining the distribution of soil-water content and formation of zones of soil saturation in these instances. Barling (1992), studying a 7-ha hillslope near Wagga Wagga in New South Wales, Australia, found that subsurface flow was affected by only a small proportion of the contributing area directly upslope during storm events and that the initial surface saturation did not occur at the points with the largest $\ln(A_s/\tan\beta)$ values.

The quasi-dynamic topographic wetness index calculated by DYNWET is an alternative index that recognizes that the subsurface flow regime in a catchment rarely, if ever, reaches steady state (i.e., that every point is experiencing drainage from its entire upslope contributing area). The index uses an effective specific catchment area A_e that is limited by the velocity of water movement and the time between wetting events. Barling et al. (1994) computed both the steady-state and quasi-dynamic topographic wetness indices for the Wagga Wagga site and compared the results with the observed distribution of soil water and locations of saturated sources areas. The results indicated that there was a low correlation between the two wetness indices ($R^2 = 0.47$) even after reasonably long drainage periods ($t \leq 120$ days) and that the measured patterns of soil-water content closely matched the distribution of the quasi-dynamic ($A_e/\tan\beta$) index. These results show how the derivation of spatially and temporally varying indices, such as the quasi-dynamic topographic wetness index calculated by DYNWET, may be useful in some landscapes, although more work is required to demonstrate their applicability in other types of landscapes.

4.5.1 Estimation Methods

DYNWET calculates both the steady-state topographic wetness index (Equation 4.40) based on A_s and the quasi-dynamic wetness index using the effective specific catchment area, A_e. The derivation of A_e starts with the kinematic wave equation for subsurface flow:

$$q = K_s \tan \beta \tag{4.56}$$

where q is the flux density or flow per unit area of the subsurface flow (m/s), K_s is the soil saturated hydraulic conductivity (m/s), and β is the slope of the impermeable boundary (which is normally assumed to be the same as the slope of the soil surface) (Beven 1981, Sloan and Moore 1984). Barling et al. (1994) showed how this equation can be used to estimate the interstitial velocity of subsurface flow:

$$v = \frac{q}{\eta} = \frac{K_s}{\eta} \tan \beta \tag{4.57}$$

where η is the effective porosity. Iida (1984) had earlier introduced the concept of time–area curves and used this equation to estimate the time required for water to travel from point E to point F along a flow line or stream tube as follows:

$$t_{EF} = \int_F^E \frac{ds}{v} = \int_F^E \frac{\eta}{K_s \tan \beta} ds \tag{4.58}$$

where s is the horizontal distance between E and F. This equation can be used to delineate isolines showing the time required for water to reach a unit width of contour for its entire upslope area. Figure 4.1 shows that for time t, the area bounded by the unit width of contour, the two orthogonal slope lines, and the isoline is defined by $a(t)$. At the maximum time, t_s (i.e., the time required to reach steady-state equilibrium), $a(t_s)$ is equal to the specific upslope area (A_s). Barling et al. (1994) have argued that the time–area concept accounts for the character of the land surface in the upslope contributing area and the time taken for subsurface drainage to redistribute soil water in a simple but physically realistic way.

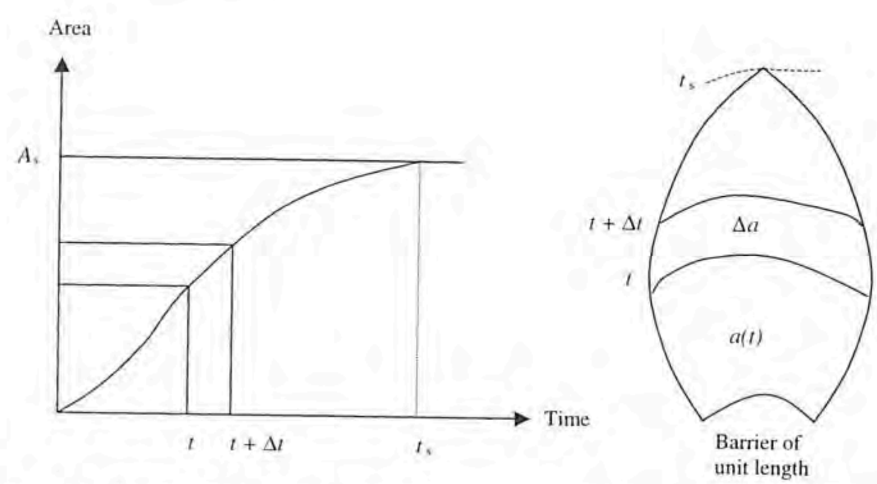

Figure 4.1. Schematic diagrams showing (a) the time–area curve, and (b) the area, $a(t)$, surrounded by the barrier, two orthogonal slope lines, and the isoline of time, t (after Iida 1984 and Barling et al. 1994).

These ideas form the basis of the quasi-dynamic topographic wetness index that is computed with DYNWET-G. The program calculates the time required for subsurface flow to travel the length of each grid cell using Equation 4.58 and a series of topographic (flow direction, slope, area) and site (drainable porosity, saturated hydraulic conductivity) attributes for each cell. The effective contributing area, A_i, for a grid cell is determined by following each drainage path in an upslope direction, accumulating travel time until it reaches the specified drainage time. The effective specific catchment area is then the ratio of A_i to flow width:

$$A_e = \frac{A_i}{b} \tag{4.59}$$

Due to the need to trace individual contributing flow paths, the more sophisticated FD8 and DEMON flow algorithms have not been implemented in DYNWET-G, so only the D8 or Rho8 flow accumulation algorithms are available for computing effective specific catchment area. The static wetness index computed by DYNWET-G uses contributing area computed by TAPES-G, so the better algorithms are available for that index.

Given this approach, DYNWET essentially extends the time–area concept first proposed and applied to a series of idealized land surfaces by Iida (1984) to grid-based representations of complex natural landscapes and offers an alternative approach for predicting soil-water content to the equilibrium approach incorporated in WET.

4.5.2 Inputs

DYNWET-G requires the output file from TAPES-G and four site parameters. The TAPES output files provide the flow direction, slope, and element area attributes. The user is asked by the program to specify the depth of soil above the impermeable layer, effective or drainable porosity, saturated hydraulic conductivity, and drainage time. The soil variables can be estimated from field measurements (as in Barling et al. 1994) or published values (as discussed with the sample application below). The drainage time is the average number of days between precipitation events and can be estimated from precipitation records at a nearby climate station.

Barling et al. (1994) examined the sensitivity of the quasi-dynamic wetness index to the choice of K_s, η, and drainage time in the Wagga Wagga study. These results showed that the predicted and measured patterns of soil water were highly correlated with the $A_e/\tan\beta$ index over a wide range of user-specified drainage times. This result occurred because the subsurface flow rates are small and the spatial distribution of the $A_e/\tan\beta$ index will not change substantially until several weeks or months have elapsed. Barling et al. (1994) also observed that the velocity of subsurface flow is directly proportional to K_s and inversely proportional to η in Equation 4.58. This structure means that the predicted wetness patterns for a specific combination of soil hydraulic properties and a user-specified drainage time will be identical to wetness patterns predicted by an equivalent set of parameters (e.g., values twice as large). Overall, these findings suggest that different input values will have a substantial impact on the time required to achieve a given wetness pattern without changing the pattern itself and that the mean patterns will not change as quickly as the absolute values (Barling et al. 1994).

4.5.3 Outputs

DYNWET-G produces an output file in either ASCII or binary form with metadata as described in Section 3.1.12. The computed topographic attributes for each DEM grid point are written as one line in an ASCII file or one unformatted record in a binary file. The attributes written to this file are summarized in Table 4.6.

4.6 SAMPLE APPLICATION

EROS, SRAD, WET, and DYNWET-G were applied to the same Cottonwood Creek catchment introduced in Chapters 2 and 3. We chose this catchment for the model runs because it was familiar to the first author and it is typical of many rangeland areas in the United States in terms of the level of environmental characterization. The terrain-analysis programs listed above were used with the 15-m DEM produced in Chapter 2, several of the topographic attributes computed from this DEM by TAPES-G in Chapter 3, and various site parameters that were obtained or estimated from published sources and/or local knowledge.

The Cottonwood Creek catchment covers approximately 197 ha and is part of the Montana State University Red Bluff Research Ranch located near Norris, MT (45°

TABLE 4.6 DYNWET Output File Fields

Field	Field Name	Units	Description
1	X	m	*x* coordinate
2	Y	m	*y* coordinate
3	Elevation	m	From DEM
4	Quasi-dynamic topographic wetness index	None	This index incorporates an effective catchment area that is a function of topography and drainage time. This approach means that most cells receive contributions from a small proportion of their total potential upslope contributing areas.
5	Steady-state topographic wetness index	None	This index assumes that the steady-state downslope subsurface discharge is the product of average discharge and specific catchment area.
6	Effective upslope contributing area	m^2	Subsurface upslope contributing area for some user-specified drainage time

33′ N, 111° 38′ W). It contains moderate to steep slopes (Figure 3.2) and the relief spans approximately 330 m (from 1642 m at the catchment outlet to 1969 m at the southeast corner of the catchment). The main channel is spring fed and runs year round. It is flanked by small, intermittent seeps that feed water laterally into this channel and several ephemeral tributaries (Aspie 1989). The soils are deep, moderately well drained, and formed in colluvium and material derived from gneiss, schist, and granite. Most of the soils have loamy or sandy loamy surface textures (Boast and Shelito 1989). The climate is semiarid (25–70 cm annual precipitation) and the vegetation is strongly correlated with landscape position and aspect. Grasses cover about 60% of the catchment and occupy south-facing slopes and ridge tops. Maple, aspen, willow, and snowberry covers about 10% of the catchment and occupy north-facing slopes and lower stream bottoms. Sagebrush interspersed with small stands of conifers dominates the remainder of the study area (Jersey 1993).

Figure 4.2 was produced in EROS using the TAPES-G outputs from Chapter 3 and by assuming uniform rainfall excess runoff. We first created a depressionless DEM in TAPES-G and then used the finite difference slope method and FD8 flow-routing method with a maximum cross-grading area of 8000 m^2 to calculate slope and specific catchment area, respectively. The uniform rainfall excess option is often chosen in EROS because no additional knowledge of runoff is required. The smallest sediment transport capacity index values occur along the catchment boundary and

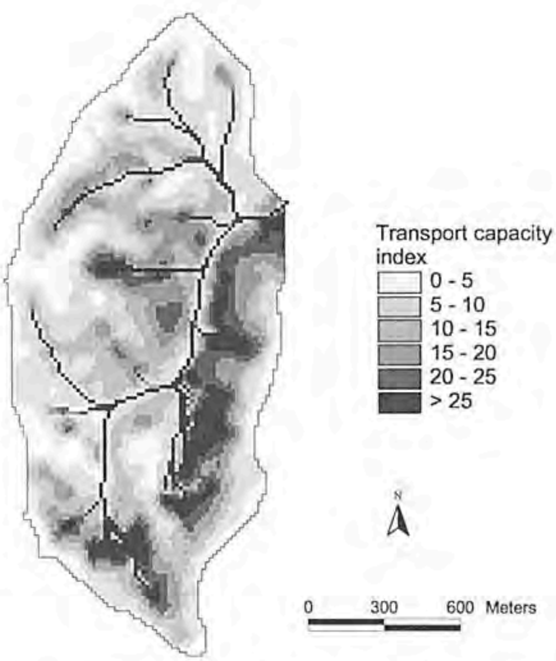

Figure 4.2. Cottonwood Creek map showing the sediment transport capacity index derived with the uniform rainfall excess runoff method in EROS.

the largest values were estimated in areas with steep slopes and large upslope contributing areas (cf. Figure 4.2 with Figures 3.2 and 3.9). Figure 4.3 shows the change in the sediment transport capacity index across hydrologically connected grid cells. Net deposition areas were predicted along footslopes and in channel areas because negative values are generated when the sediment transport capacity index decreases from one hydrologically connected cell to the next (when moving down the slope). These conditions were predicted in a few other locations along the western boundary and in the southeast corner of the catchment as well (Figure 4.3).

The next pair of diagrams shows why these types of predictions must be used with great care. The patterns shown in Figures 4.2 and 4.3 may not help much with the description of erosion and deposition in this catchment because local observations and monitoring conducted over several years suggest that saturated overland flow is the dominant runoff producing mechanism (e.g., Pogacnik 1985, Aspie 1989). Aspie (1989) measured stream flow at two flumes (labeled B and F in Figure 4.5) for 10 storm events in 1986 and 1987. No saturated zones were observed above flume B. Channel areas constituted 0.8% of this zone. Numerous saturated areas were observed between flumes B and F and these areas combined with the channel constituted 1.6% of this zone. Aspie (1989) explained 80–90% of the storm runoff volumes measured at the two flumes by assuming that all of the precipitation falling on these areas was converted to storm runoff. A critical wetness index of 8.5 was derived from

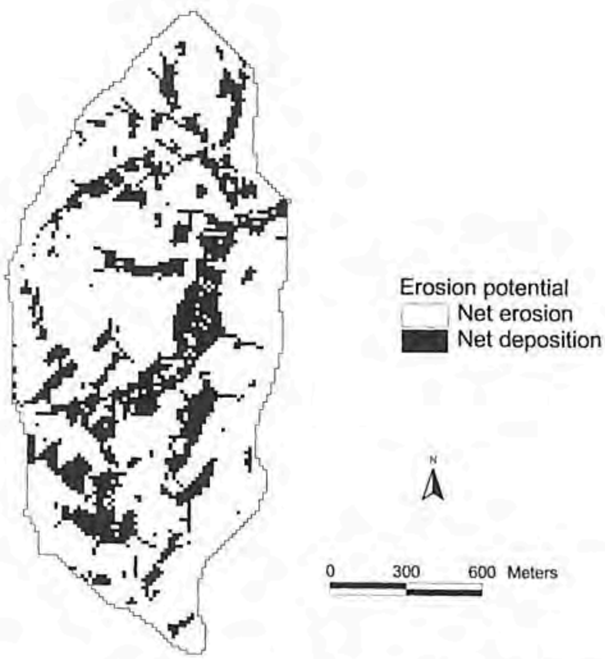

Figure 4.3. Cottonwood Creek map showing the change in sediment transport capacity index derived with the uniform rainfall excess runoff method in EROS.

the cumulative frequen
in Figure 4.4 by assun
storm runoff; the index
map produced a very d
in Figure 4.2 and the d
ate runoff method for tl
ure 4.5 identify low a
generate saturated ovei
catchment dominated b
steep slopes with larg
located just east of the
The radiation and te
using SRAD, the 15-m
file (Table 4.7). Thirty
Bozeman W6 Experim
temperature inputs, res
study area is the only
National Solar Radiati
stations. Primary statio

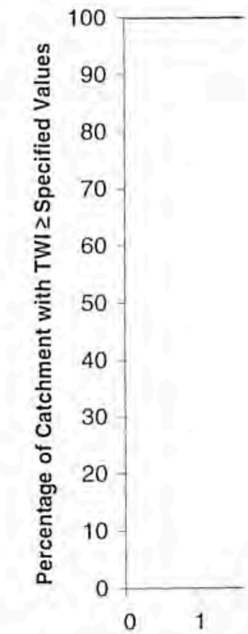

Figure 4.4. Cumulative
the Cottonwood Creek ca

the cumulative frequency plot of steady-state topographic wetness index reproduced in Figure 4.4 by assuming that approximately 5% of the catchment contributes to storm runoff; the index was used to generate the map reproduced in Figure 4.5. This map produced a very different spatial pattern compared to the first map reproduced in Figure 4.2 and the differences highlight the importance of choosing the appropriate runoff method for the area of interest when using EROS. The shaded areas in Figure 4.5 identify low areas with large upslope contributing areas that are likely to generate saturated overland flow. The cells with zero values show those parts of the catchment dominated by lateral subsurface flow. No overland flow is predicted on the steep slopes with large sediment transport capacity values in Figure 4.2 that are located just east of the main channel in this instance (c.f. Figures 4.2 and 4.5).

The radiation and temperature attributes summarized in Table 4.3 were calculated using SRAD, the 15-m DEM from Chapter 2, and the Madison Range site parameter file (Table 4.7). Thirty-year (1961–1990) monthly records from the Great Falls and Bozeman W6 Experiment Farm climate stations were used to estimate radiation and temperature inputs, respectively. The Great Falls station located 220 km north of the study area is the only primary solar radiation station located in Montana. The U.S. National Solar Radiation Database contains 56 primary stations and 183 secondary stations. Primary stations report measured solar radiation data for at least a portion of

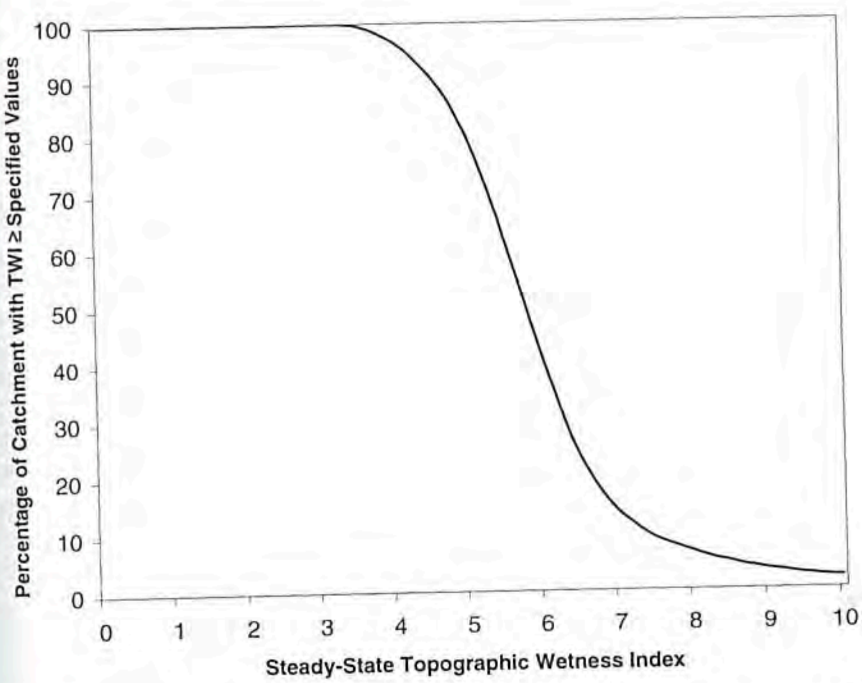

Figure 4.4. Cumulative frequency distribution of steady-state topographic wetness index in the Cottonwood Creek catchment.

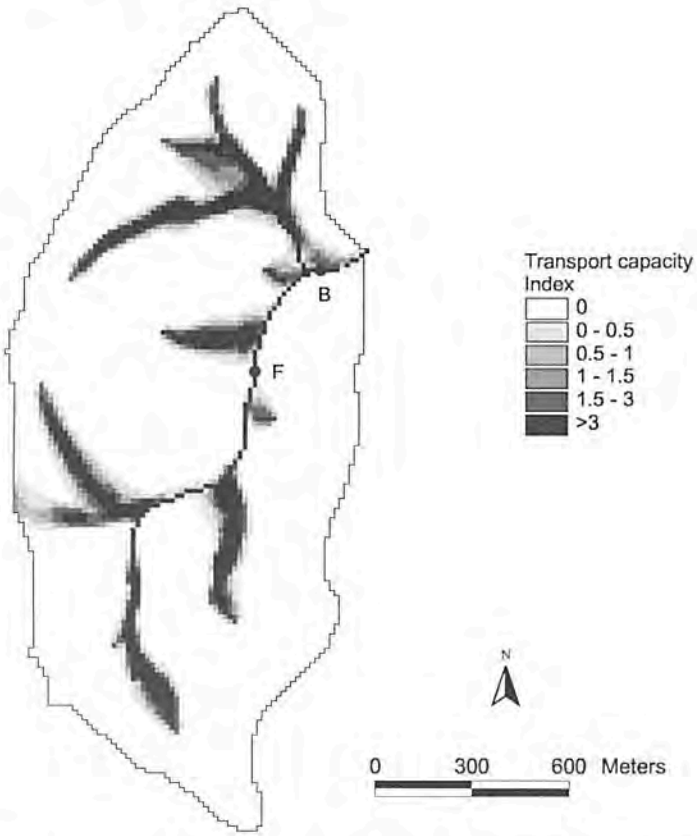

Figure 4.5. Cottonwood Creek map showing the sediment transport capacity index derived with the saturated overland flow runoff method in EROS.

their 30-year record and secondary stations contain modeled solar radiation data (National Renewable Energy Laboratory 1992). The circumsolar, cloud transmittance, and lumped transmittance coefficients were estimated with the equations listed in Section 4.3.2 and the sunshine hours and radiation fluxes reported for this station.

The Bozeman W6 Experiment Farm climate station is located 22 km east of the study area and was chosen because it is the closest station with long-term air and surface (soil) temperature measurements (Munn et al. 1981). Mean monthly minimum and maximum air temperatures were obtained directly from station records and the three sets of lapse rates were estimated with the modified version of the spatial filtering-kernal convolution method described in Section 4.3.2. Mean monthly soil temperatures were reported at depths of 5 or 10 cm for the period 1981–1990 and these data were used to estimate mean monthly temperature gradients and surface temperatures. The recorded temperatures were adjusted for depth on a monthly basis because seasonal variations in soil temperatures are greatest at the surface and

TABLE 4.7 Madison Range SRAD Site Parameter File

45.22	45.22										
0.07	0.10	0.12	0.14	0.16	0.19	0.23	0.20	0.16	0.12	0.08	0.07
0.59	0.57	0.57	0.37	0.19	0.14	0.14	0.14	0.18	0.28	0.49	0.56
0.31	0.30	0.27	0.28	0.28	0.28	0.20	0.22	0.27	0.29	0.32	0.32
0.49	0.56	0.66	0.62	0.62	0.65	0.79	0.76	0.67	0.61	0.46	0.44
0.2	3.1	6.9	12.7	17.9	23.1	27.6	27.1	21.2	14.4	5.6	0.7
−11.6	−8.9	−5.6	−1.4	2.9	6.8	9.3	8.6	4.1	−0.4	−6.2	−11.1
−1.9	−1.8	0.6	5.8	12.2	18.3	24.0	24.3	13.8	7.2	1.5	−1.3
3.9	4.8	6.2	7.1	8.0	6.4	6.2	4.3	6.4	6.5	4.6	4.5
2.5	3.8	5.2	5.2	5.6	4.5	4.4	2.5	3.9	4.1	3.1	3.2
4.8	5.4	6.9	8.3	9.5	7.7	7.4	5.5	8.0	8.0	5.6	5.3
1											
0.2	0.2	0.2	0.5	1.5	2.5	2.5	1.5	1.0	0.5	0.2	0.2
10.0	0.98	0.00008	1455.4								
0.64	0.66	0.63	0.64	0.65	0.68	0.67	0.65	0.65	0.64	0.67	0.65

Note. See Table 4.2 for description of variables recorded in individual rows and columns.

decrease with depth until, at a depth of 10 m or more, they disappear (Smith et al. 1964, Parton and Logan 1981). The land cover information recorded with station temperature measurements may also be important because soil temperatures can be expected to vary with land cover: Munn et al. (1978), for example, found that soil temperatures differed significantly in adjacent high elevation forests and meadows in Montana. The parameter values used to describe the surface conditions in Table 4.7 were derived from published values for midlatitude range sites.

Maps of the net annual solar radiation, net solar radiation in winter and summer, short-wave solar radiation ratio, and mean annual average temperature are reproduced in Figures 4.6–4.8. The net annual solar radiation map shows the major geomorphic features of the catchment. The largest net annual solar radiation values (>10 W/m^2) occur on the south-facing slopes that delineate the northern boundary of the catchment and on the large south-facing slope that dominates the center of the catchment (Figure 4.6). Low values (<10 W/m^2) are predicted on those parts of the catchment with north-facing slopes and/or in areas shaded for part of the day by the surrounding landscape. The net annual solar radiation values reported in Figure 4.6 vary between −19.5 and 15.9 W/m^2, and the mean value of −1.1 W/m^2 indicates that large negative values were slightly more prevalent than positive values. The spatial pattern more or less matches that produced for the short-wave solar radiation index (see Figure 4.8a). This particular map shows the ratio of incident short-wave radiation for each grid point compared to a horizontal point at the same latitude with no topographic shading. Approximately 7.2% of the cells have ratios greater than 1.1 (i.e., they signify south-facing slopes) and 45.4% have ratios less than 0.9 (these cells signify north-facing slopes and/or sites that experience topographic shading). Both of these maps therefore illustrate the impact of surrounding terrain in modifying the radiation budget at specific sites within a catchment.

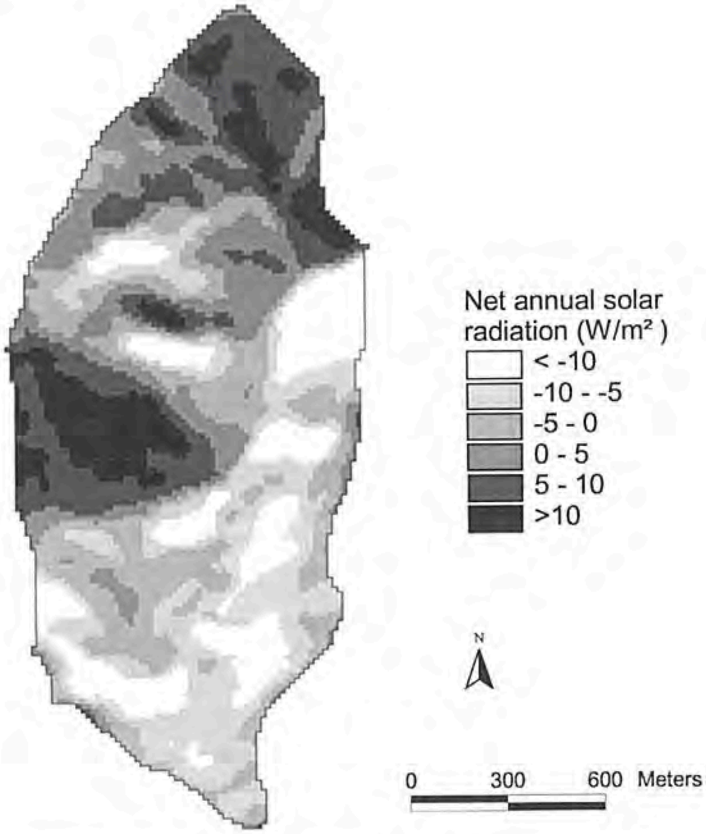

Figure 4.6. Cottonwood Creek net annual solar radiation map.

The same general patterns are repeated in the winter (December–February) and summer (June–August) net solar radiation maps reproduced in Figure 4.7. These maps show net irradiance in six equal area classes. The summer values are much larger than the winter values (144.6 versus –42.3 W/m^2 mean net irradiance) and the spatial patterns are slightly different in areas influenced by topographic shading because of the impact of varying sun angles at these latitudes at different times of the year. Regressing winter net solar radiation against summer net solar radiation produced an R^2 of 0.74 and illustrates how the impact of surrounding terrain in modifying the radiation budget at specific sites is likely to vary seasonally in midlatitude areas such as Cottonwood Creek. The greater variability evident in summer (Figure 4.7b) compared to winter (Figure 4.7.a) is largely a function of magnitude since the coefficient of variation in summer (0.10) is about half as large as that recorded in winter (0.16). The winter values varied from –52.1 to –25.4 W/m^2 (–42.3 W/m^2 mean) and the summer values varied from 102.8 to 167.4 W/m^2 (144.7 W/m^2 mean). These mean catchment values are consistent with the December and June net irradiance estimates reported for southwest Montana by Budyko (1974). Further validation

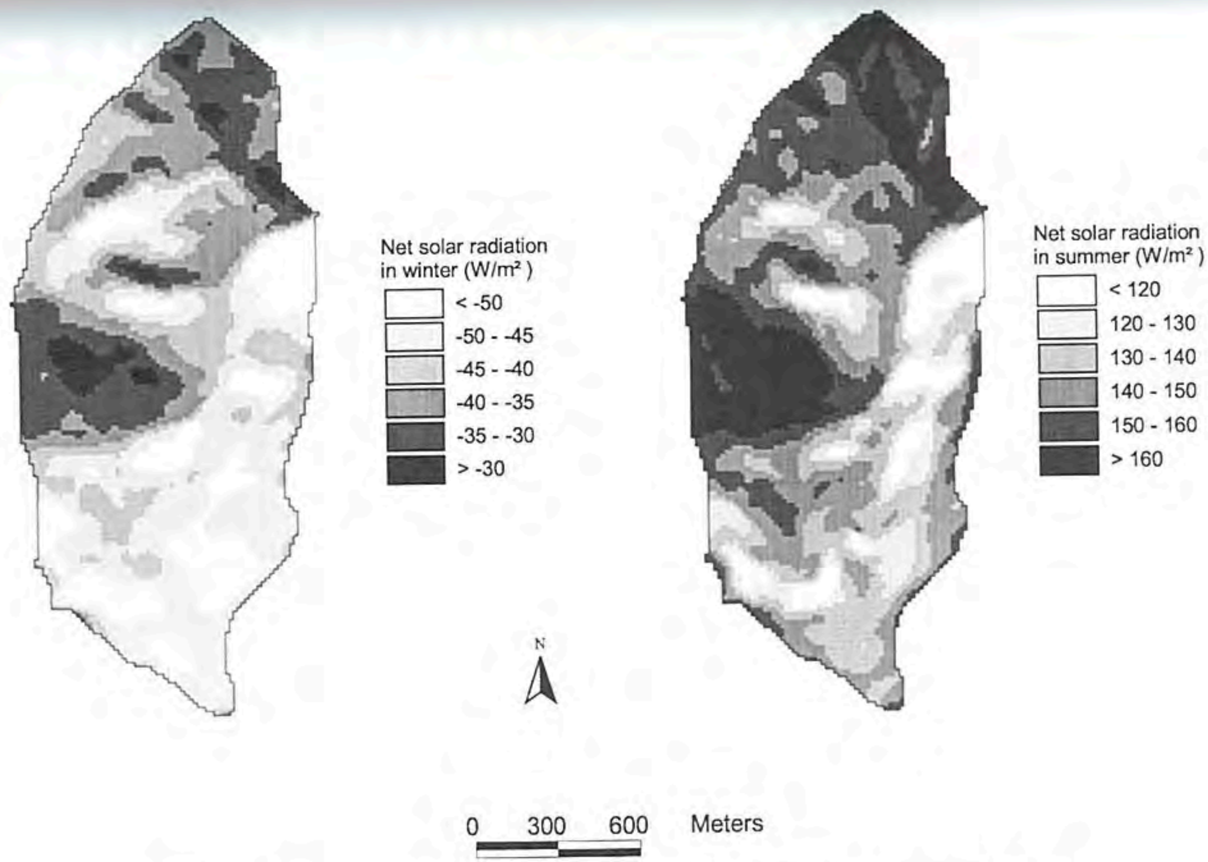

Figure 4.7. Cottonwood Creek maps showing (a) net solar radiation in winter and (b) net solar radiation in summer.

was not possible because of the paucity of radiation measurements for horizontal and especially sloping terrain in this region, and the SRAD user can assume that this situation is typical of most other parts of the world as well.

The mean annual average air temperature map reproduced in Figure 4.8b combines the effects of elevation (via the lapse rate) and slope, aspect, and topographic shading (via the short-wave solar radiation index) (Figure 4.8a). Elevation ranged from 1642 to 1969 m and coincided with the locations of relatively high (5.1°C) and low (3.3°C) predicted temperatures, respectively. The highest mean annual average air temperature (5.3°C) was computed at two points with similar elevations (1651 and 1656 m) and short-wave radiation ratios (0.941 and 0.963 respectively). The low temperature (3.0°C) was computed at a point with an elevation of 1821 m and short-wave radiation ratio of 0.983.

The three soil-water content maps reproduced in Figure 4.9 were produced with the three sets of estimation techniques available in WET. The first map utilized a critical steady-state topographic wetness index value of 7.5 and $(E + D)/P$ ratio of 0.90 (i.e., we assumed that 90% of the precipitation was lost from the soil via deep drainage and evapotranspiration and not converted to runoff). The relative soil-water content varied from 0.12 to 1.0 in this instance and the map shows that the higher values generally occurred in cells with large upslope contributing areas (Figure 4.9a). This particular approach (map) assumes that topography controls relative soil-water content and the pattern mimics that shown for the steady-state topographic wetness index in Figure 4.10a.

The relative soil-water content map reproduced in Figure 4.9b was computed with the level 2 estimation techniques and the site parameters listed in Table 4.8. These values ranged from 0.38 to 1.0 and produced subtle variations in spatial patterns compared to the level 1 map. The relative soil water content values predicted with the level 2 estimation methods were approximately 50% larger on average than those predicted with level 1 (i.e., mean relative soil-water content values of 0.45 and 0.69 were predicted in Figure 4.9a and b, respectively). This pair of maps also shows that slightly different patterns were predicted in cells that experienced substantial topographic shading and therefore lower rates of evapotranspiration losses (as illustrated by the steep slopes to the east of the main channel and on north-facing slopes scattered throughout the study area). The final map reproduced in Figure 4.9c was generated with the level 3 estimation techniques and site parameters listed in Table 4.8. This map contains slightly larger values than the second map (0.40, 0.71, and 1.0 minimum, mean and maximum values, respectively) because the rate of loss to deep drainage and evapotranspiration were partially controlled by the relative soil-water content in this instance. The choice of study area and site parameters, however, meant that these differences were very small and the spatial patterns produced with the level 2 and level 3 estimation techniques are very similar.

The last pair of maps reproduced in Figure 4.10 show the steady-state and quasi-dynamic topographic wetness indices calculated with DYNWET-G. The steady-state topographic wetness index (Figure 4.10a) is similar to the WET level 1 soil-water content map (Figure 4.9a) but for the fact that no critical wetness index was specified and used to normalize the computed cell values. These values vary from 4.7 to 14.9

ents for horizontal and
ın assume that this sit-

d in Figure 4.8b com-
spect, and topographic
.8a). Elevation ranged
ively high (5.1°C) and
t mean annual average
milar elevations (1651
respectively). The low
n of 1821 m and short-

.9 were produced with
first map utilized a crit-
$(E + D)/P$ ratio of 0.90
rom the soil via deep
The relative soil-water
ows that the higher val-
ng areas (Figure 4.9a).
trols relative soil-water
te topographic wetness

.9b was computed with
ted in Table 4.8. These
ions in spatial patterns
alues predicted with the
on average than those
values of 0.45 and 0.69
of maps also shows that
enced substantial topo-
on losses (as illustrated
orth-facing slopes scat-
in Figure 4.9c was gen-
eters listed in Table 4.8.
ap (0.40, 0.71, and 1.0
the rate of loss to deep
y the relative soil-water
e parameters, however,
patterns produced with

steady-state and quasi-
VET-G. The steady-state
WET level 1 soil-water
ness index was specified
es vary from 4.7 to 14.9

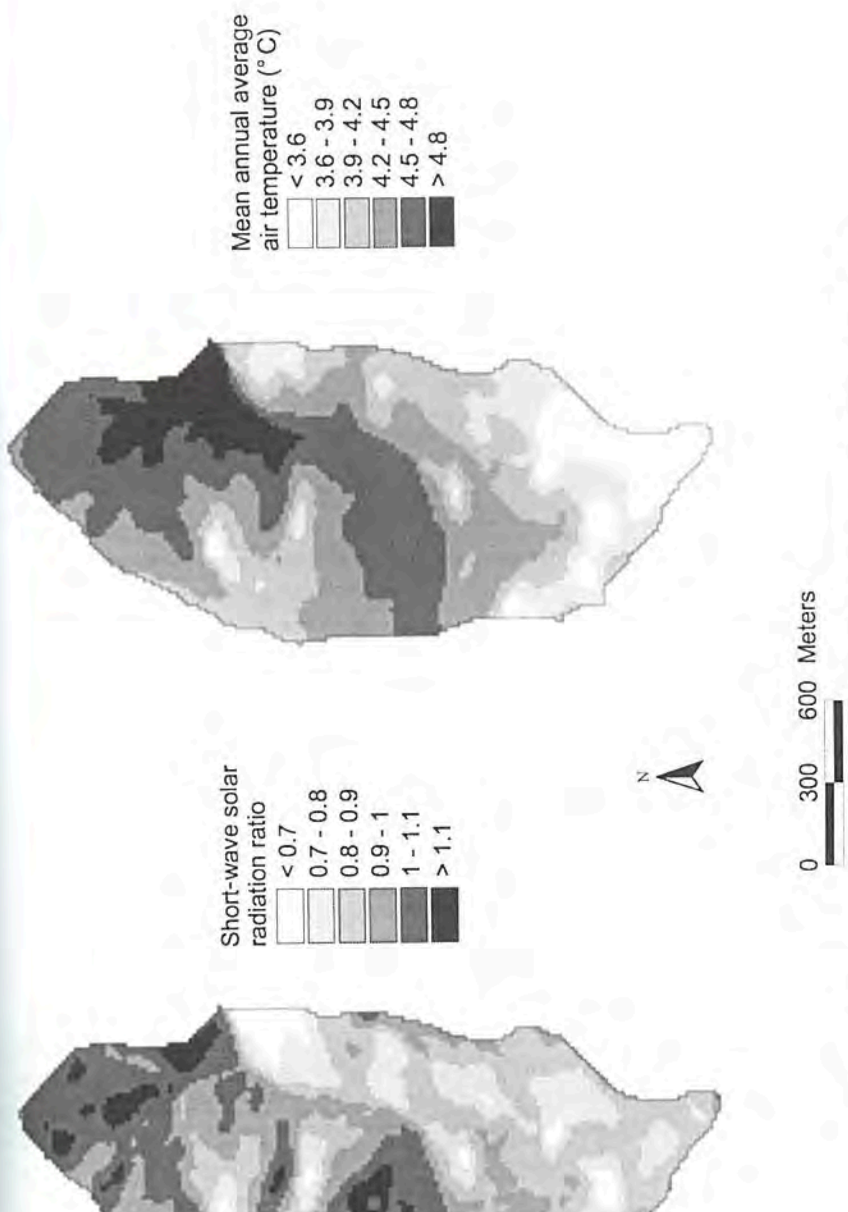

Figure 4.8. Cottonwood Creek maps showing (a) the short-wave solar radiation ratio and (b) mean annual average air temperature.

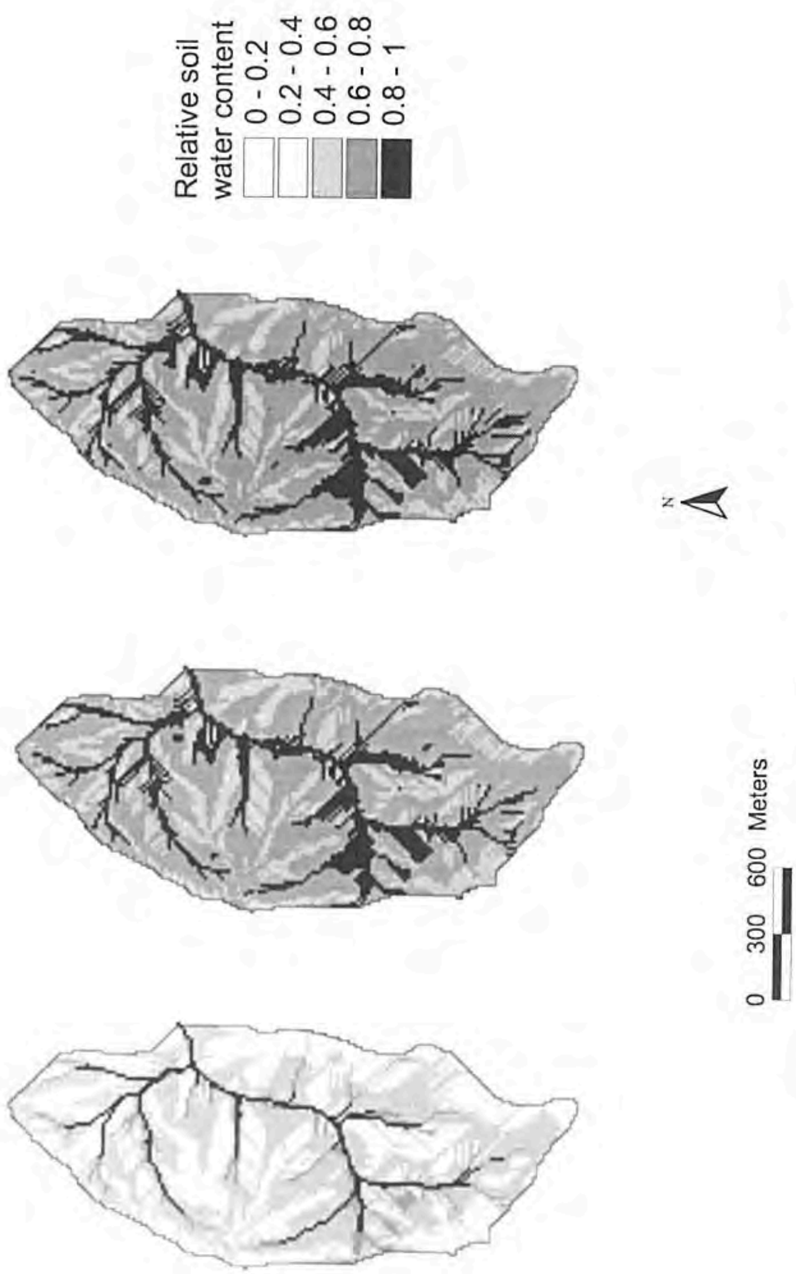

Figure 4.9. Cottonwood Creek maps of relative soil-water content derived with the three sets of estimation techniques available in WET.

TABLE 4.8 Madison l

Parameter
Critical wetness index, χ_{cr}
Mean air temperature (°C)
Mean elevation (m)
Precipitation (mm/day)
Interception losses (mm/day)
Maximum drainage rate D_{max} (mm/day)
β
C
$(E + D)/P$ ratio

and the mean compute
itively skewed (as is the
the quasi-dynamic topo
ment compared to the s
The quasi-dynamic top
mean is 5.1. The large
hollows in higher elev
immediately above gen

The quasi-dynamic t
and user-specified soil
and drainage time value
The mean weighted soi
soil mapping units and
The mean weighted dra
by Boast and Shelito (1
lished data specifying t
et al. 1983). The mean v
similar fashion with the
eter by soil texture class
by a factor of 3 to acco
sents the spacing betwee
saturated hydraulic cond
tive upslope contributin
parameters used in this
and 158 m on 10 and 6
place of the generalized
dynamic topographic w
also required to evaluat

TABLE 4.8 Madison Range WET Site Parameter File

Parameter	Level 1	Level 2	Level 3
Critical wetness index, χ_{cr}	7.5	7.5	7.5
Mean air temperature (°C)	—	5.6	5.6
Mean elevation (m)	—	1652	1652
Precipitation (mm/day)	—	1.52	1.52
Interception losses (mm/day)	—	0.18	0.18
Maximum drainage rate D_{max} (mm/day)	—	0.15	0.15
β	—	10	10
C	—	—	12
$(E + D)/P$ ratio	0.90	—	—

and the mean computed for the catchment (6.5) shows that the distribution was positively skewed (as is the case in most catchments) (Figure 4.10a). Figure 4.10b shows the quasi-dynamic topographic wetness index and a subtly different spatial arrangement compared to the steady-state topographic wetness index map in Figure 4.10a. The quasi-dynamic topographic wetness index values vary from 3.4 to 6.7 and the mean is 5.1. The largest quasi-dynamic index values are predicted in topographic hollows in higher elevations (i.e., in local areas with convergent flow lines) and immediately above gently sloping areas near channels (i.e., on footslopes).

The quasi-dynamic topographic wetness index was computed with the same DEM and user-specified soil depth, drainable porosity, saturated hydraulic conductivity, and drainage time values of 1.3 m, 0.4 cm^3/cm^3, 200 mm/h, and 20 days, respectively. The mean weighted soil depth was estimated from the spatial extent of the different soil mapping units and published soil series descriptions (Boast and Shelito 1989). The mean weighted drainable porosity was estimated from soil texture data reported by Boast and Shelito (1989) (weighted by spatial extent and depth) and some published data specifying typical drainable porosity values by soil texture class (Ratliff et al. 1983). The mean weighted saturated hydraulic conductivity was estimated in a similar fashion with the help of published data reporting typical values of this parameter by soil texture class (Rawls and Brakensiek 1989) and multiplying this estimate by a factor of 3 to account for rapid subsurface pathways. The drainage time represents the spacing between major precipitation and/or snowmelt events and along with saturated hydraulic conductivity and effective porosity controls the size of the effective upslope contributing area that is calculated for each cell in DYNWET-G. The parameters used in this instance predicted maximum travel times (distances) of 24 and 158 m on 10 and 66% slopes, respectively. The use of local site parameters in place of the generalized estimates used here is likely to alter (improve?) the quasi-dynamic topographic wetness index calculated with DYNWET-G. These data are also required to evaluate how well the steady-state and quasi-dynamic topographic

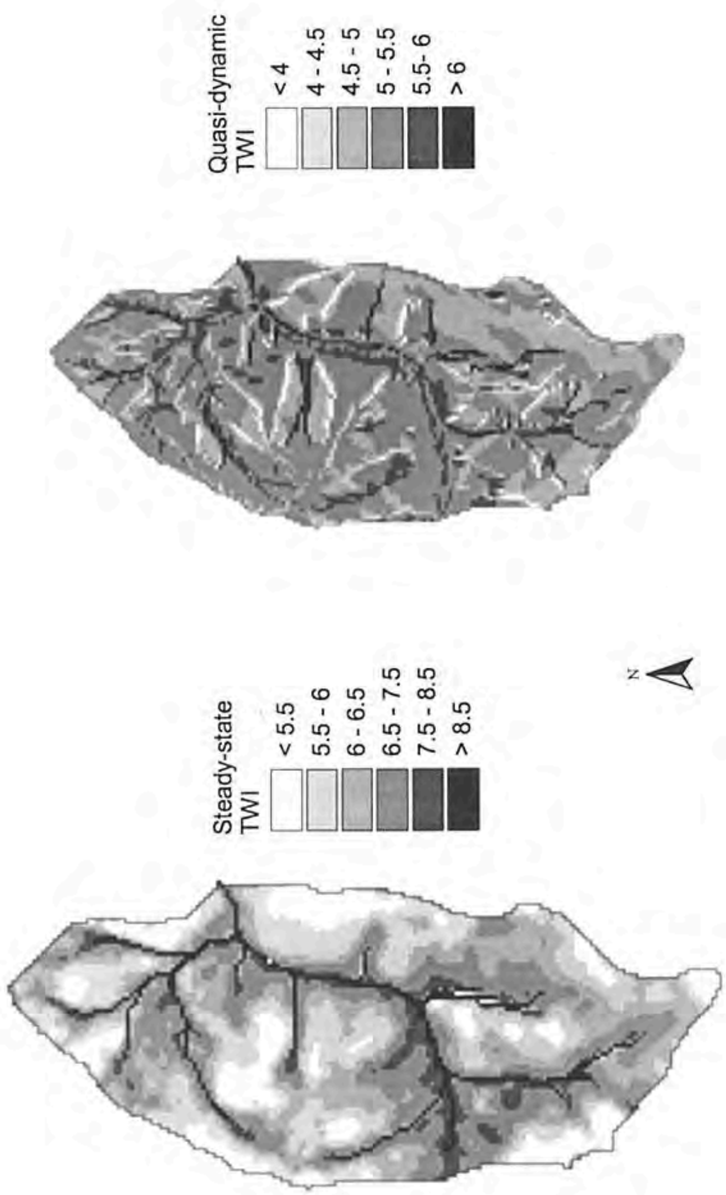

Figure 4.10. Cottonwood Creek maps showing (a) steady-state topographic wetness index and (b) quasi-dynamic topographic wetness index.

wetness indices are able
in this catchment.

4.7 CONCLUSIONS

Topographic maps are a
graphic attributes and pl
itoring, soil survey, and
data become available, t
based indices. For exam
sion can initially be esti
information becomes av
as information on vege
model that accounts for
Mitasova et al. 1996). T
processes can be model
data being developed ov
utes constituting a mini
from a digital elevation
Most GIS are based on a
rain analysis can provid
integrated within their a

The foregoing discus
and DYNWET-G indica
basic approach relies
processes and it is desig
ulate the system's behav
assumed to have low var
some physical sophistica
scapes (I. D. Moore et a
level of available data an
tions need, and can, be
Barling et al. 1994). Mos
topographic indices calc
phological, and biologic

Figure 4.10. Cottonwood Creek maps showing (a) steady-state topographic wetness index and (b) quasi-dynamic topographic wetness index.

wetness indices are able to represent topographic controls on soil-water distribution in this catchment.

4.7 CONCLUSIONS

Topographic maps are available in most countries and can be used to calculate topographic attributes and plan additional data collection networks for hydrological monitoring, soil survey, and biological survey applications. As additional environmental data become available, they can be used to provide improved estimates of the terrain-based indices. For example, the susceptibility of the landscape to sheet and rill erosion can initially be estimated using only topographic data. As hydrological and soils information becomes available, it can be integrated into the predictions; and finally, as information on vegetation and cover is developed, a physically based erosion model that accounts for detachment and transport processes can be utilized (e.g., Mitasova et al. 1996). The radiation, temperature, evapotranspiration, and soil-water processes can be modeled in similar ways. We therefore visualize different layers of data being developed over time with elevation data and the related topographic attributes constituting a minimum data set. Topographic attributes can be easily estimated from a digital elevation model using any one of a number of terrain analysis methods. Most GIS are based on a pixel or cellular structure so that grid-based methods of terrain analysis can provide the primary geographic data for them and can be easily integrated within their analysis subsystems.

The foregoing discussion of the methods incorporated in EROS, SRAD, WET, and DYNWET-G indicates why care is needed when applying these techniques. The basic approach relies on simplified representations of the underlying physical processes and it is designed to include the key factors, such as topography, that regulate the system's behavior. Factors that are not explicitly included in an index are assumed to have low variance within the landscape. With this approach, we sacrifice some physical sophistication to allow improved estimates of spatial patterns in landscapes (I. D. Moore et al. 1991, 1993f). This approach will be consistent with the level of available data and the precision with which many of the management questions need, and can, be answered in many instances (Moore and Hutchinson 1991, Barling et al. 1994). Most of the chapters that follow explore how one or more of the topographic indices calculated with these tools can be used in hydrological, geomorphological, and biological applications.